The role of equatorial waves in triggering precipitation extremes in the Maritime Continent

Article

Published Version

Open Access

It is advisable to refer to the publisher's version if you intend to cite from the work. See Guidance on citing.

To link to this article DOI: http://dx.doi.org/10.1175/MWR-D-25-0073.1

www.reading.ac.uk/centaur

CentAUR

Central Archive at the University of Reading

Reading's research outputs online

∂The Role of Equatorial Waves in Triggering Precipitation Extremes in the Maritime Continent

Beata Latos,[a] Samantha Ferrett,[b,c] Thierry Lefort,[d] Adrian J. Matthews,[e] Sandro W. Lubis,[f]
Natasha V. Senior,[e] Philippe Peyrillé,[g] Hanh Nguyen,[h] Matthew C. Wheeler,[h] Jeong-Yik Diong,[i]
Dariusz B. Baranowski,[j] Maria K. Flatau, Piotr J. Flatau,[k] Ida Pramuwardani,[l]
Fadhlil R. Muhammad,[m,n] Donaldi S. Permana,[l] Muhamad R. Ferdiansyah,[l] Agie Wandala,[k] Kiki,[l]
Idhan Abubakar,[l] Tito Praditya,[l] Eddy Hermawan,[o] and Jacek Piskozub[a]

[a] Institute of Oceanology Polish Academy of Sciences, Sopot, Poland
[b] National Centre of Atmospheric Science, University of Reading, Reading, United Kingdom
[c] Department of Meteorology, University of Reading, Reading, United Kingdom
[d] Forecasting Division, Météo-France, Toulouse, France
[e] Centre for Ocean and Atmospheric Sciences, School of Environmental Sciences, University of East Anglia, Norwich, United Kingdom
[f] Pacific Northwest National Laboratory, Richland, Washington
[g] Centre National de Recherches Météorologiques, Université de Toulouse, Météo-France, CNRS, Toulouse, France
[h] Bureau of Meteorology, Melbourne, Victoria, Australia
[i] Malaysian Meteorological Department, Petaling Jaya, Malaysia
[j] Institute of Geophysics Polish Academy of Sciences, Warsaw, Poland
[k] Scripps Institution of Oceanography, University of California, San Diego, San Diego, California
[l] Indonesian Agency for Meteorology, Climatology, and Geophysics (BMKG), Jakarta, Indonesia
[m] School of Geography, Earth and Atmospheric Sciences, The University of Melbourne, Melbourne, Victoria, Australia
[n] ARC Centre of Excellence for the Weather of the 21st Century, The University of Melbourne, Melbourne, Victoria, Australia
[o] National Research and Innovation Agency (BRIN), Jakarta, Indonesia

ABSTRACT: This review offers a comprehensive analysis of convectively coupled equatorial waves (CCEWs) and their pivotal role in driving precipitation extremes across the Maritime Continent. It examines the current understanding of CCEWs, evaluates the performance of numerical models and forecasting techniques in predicting these phenomena, and pinpoints critical areas for improvement. The discussion centers on three key types of equatorial waves: equatorial Rossby waves, Kelvin waves, and mixed Rossby–gravity waves. By connecting scientific insights with practical forecasting applications, the review sheds light on the challenges of predicting these waves while identifying opportunities to advance both fundamental knowledge and forecasting accuracy. Designed as an educational resource, it targets operational forecasting centers, meteorologists, and researchers, aiming to enhance the prediction of extreme weather events in the region.

SIGNIFICANCE STATEMENT: Rainfall extremes in the Maritime Continent are among the most intense on Earth, posing major challenges for both society and weather forecasting. This review highlights the crucial role of convectively coupled equatorial waves—large-scale tropical weather systems—in triggering such events. Through both their direct influence and interactions with the diurnal rainfall cycle and other weather systems, equatorial waves amplify precipitation and create favorable conditions for extreme rainfall. Despite their important role in modulating precipitation extremes, they are still underrepresented in many numerical weather prediction models, limiting forecast accuracy. Improving understanding and representation of these waves offers a pathway toward better forecasts and greater resilience in one of the world's most vulnerable and rain-prone regions.

1. Introduction

The Maritime Continent (MC), an archipelago between the Indian and Pacific Oceans, experiences the world's highest precipitation, leading to weather-related risks including extreme rainfall, floods, and landslides. Factors such as increasing population density, land-use changes, deforestation, and climate change increase vulnerability to weather extremes (Measey 2010; Muis et al. 2015; Moe et al. 2017; Yamamoto et al. 2021).

Convectively coupled equatorial waves (CCEWs) are large-scale, coherent weather systems that move either eastward or westward within the tropics (Wheeler and Kiladis 1999; Kiladis et al. 2009). They operate on time scales intermediate between longer-term variability such as El Niño–Southern Oscillation

Corresponding author: Beata Latos, blatos@iopan.pl

(ENSO) (Aldrian and Dwi Susanto 2003; Jia et al. 2016; Zhang et al. 2016), the Indian Ocean dipole (IOD) (Saji et al. 1999; Schott et al. 2009; Nur'utami and Hidayat 2016), and the Madden–Julian oscillation (MJO) (Madden and Julian 1972; Wheeler and Hendon 2004; Peatman et al. 2014; Birch et al. 2016; Muhammad et al. 2021; Da Silva and Matthews 2021) and shorter-term phenomena including mesoscale convective systems, the diurnal cycle, and individual cumulonimbus (Birch et al. 2016; Sakaeda et al. 2020; Peatman et al. 2021; Karlowska et al. 2024; Peatman et al. 2014; Yamanaka et al. 2018; Mustafa et al. 2025).

Within the multiscale interaction framework of tropical meteorology (Meehl et al. 2001), CCEWs are often embedded within and influenced by larger-scale convective envelopes associated with ENSO and IOD (Meehl et al. 2001; Moron et al. 2015; Yamanaka 2016; Yoneyama and Zhang 2020; Saufina et al. 2025; Aslam 2025). Understanding these interactions is critical for the MC, where CCEWs contribute significantly to precipitation variability. These waves also interact with the MJO at intraseasonal time scales, modulating convection (Lubis and Jacobi 2015; Majda et al. 2004; Kikuchi et al. 2018; Geng and Katsumata 2021; Muhammad et al. 2024; Suhas and Neena 2025). The MJO provides a large-scale convective envelope that strongly modulates CCEWs, with convection enhanced over the MC when the MJO convective center is located over the region, thereby favoring CCEW activity (Zhu and Li 2021; Roundy 2008).

Despite their importance, current literature provides no robust quantitative assessment of how large-scale modes of variability interact with CCEWs over the MC. Nonetheless, several studies suggest contrasted responses depending on the type of wave and the background state. For instance, El Niño is associated with a marked reduction in equatorial Rossby and mixed Rossby–gravity wave activity (Huang and Huang 2011), whereas the response of Kelvin waves remains less conclusive, showing only a weak reduction overall but with clear seasonal and regional dependencies (Huang and Huang 2011; Yang and Hoskins 2016; Rakhman et al. 2017). It should also be noted that all CCEWs show seasonal variations in their activity (Kiladis et al. 2009), arising from interactions with the background flow. In the MC region, this interaction also results in spatial differences in CCEW activity.

While variations in CCEW activity have often been related to vertical wind shear and background circulation (Yang and Hoskins 2016), humidity and convection are equally critical modulators (Rakhman et al. 2017; Zhu and Li 2021). This highlights the need to consider the full spectrum of variability when analyzing CCEW dynamics over the MC, and advancing our understanding requires further research to quantify the sensitivity of CCEWs to large-scale convective variability.

At the same time, CCEWs help create an environment conducive to the development of smaller-scale mesoscale convective systems (Diong et al. 2023; Trismidianto et al. 2023; Cheng et al. 2023). The interaction, interdependence, and complex coexistence of these phenomena make rainfall forecasting over the MC particularly challenging. Recent studies highlight CCEWs as key triggers of weather extremes in the MC (Ferrett et al. 2020; Lubis and Respati 2021; Latos et al. 2023). Major flood events in

Jakarta (Lubis et al. 2022), Padang (Baranowski et al. 2020; Senior et al. 2023), Pontianak (Senior et al. 2025), and Makassar (Latos et al. 2021; Doyle et al. 2023) were linked to equatorial waves, underscoring the need to integrate these insights into forecasting. While MJO and equatorial waves have long been monitored globally (Wheeler and Weickmann 2001; Molinari et al. 2006), based on discussions at the Wavy-Tropics Workshop (November 2023, Jakarta, and online; https://www.wavytropics.com), their application in MC forecasts appears to remain limited, despite their potential to improve predictions.

Global numerical weather prediction (NWP) models struggle with local-scale rainfall in the tropics due to limitations in convection parameterization (Gehne et al. 2022; Birch et al. 2016; Dias et al. 2018; Baranowski et al. 2019; Argüeso et al. 2020). Additionally, sparse observational coverage in the tropics limits the quality of initial conditions, further constraining forecast accuracy (Bauer et al. 2015). While large-scale drivers can be predicted weeks ahead, the precise timing and location of extreme precipitation remain an ongoing challenge. Operational models now predict the MJO with 3–4-week lead times (Klingaman and Woolnough 2014; Kim et al. 2014), while equatorial waves allow shorter-range forecasts within days to a week (Baranowski et al. 2020; Yang et al. 2021). Over the past two decades, forecasting accuracy has improved due to better representation of equatorial waves (Dias et al. 2023). Additionally, artificial intelligence (AI)-based models such as GenCast (Price et al. 2025), GraphCast (Lam et al. 2023), and Pangu-Weather (Bi et al. 2023) show promise for medium-range forecasting (up to 10–15 days). These models have demonstrated competitive skill with traditional NWP systems while being computationally efficient. However, their performance for tropical convective processes and extreme precipitation events is still being evaluated, and challenges remain in representing rare events and physical consistency (Reichstein et al. 2019; Price et al. 2025). As AI-based methods continue to develop, they are expected to complement traditional NWP approaches and enhance operational forecasting capabilities in the coming years.

This review provides a comprehensive analysis of CCEWs, emphasizing their role in driving precipitation extremes in the MC. It summarizes current knowledge, evaluates model accuracy, addresses forecasting challenges, and suggests future research improvements. Section 2 examines CCEWs as drivers of extremes, covering theory, Rossby waves, Kelvin waves, and mixed Rossby–gravity waves. Unlike studies that review theoretical wave patterns (Kiladis et al. 2009) and tracking methods (Knippertz et al. 2022), this section places a stronger emphasis on precipitation extremes. Section 3 assesses forecasting equatorial waves and precipitation in the MC, addressing challenges and model representation. Section 4 suggests future improvements, exploring model enhancements and practical forecasting tools. Finally, section 5 presents the concluding remarks. A comprehensive table of acronyms is provided in appendix A for easy reference.

2. Equatorial waves: A review regarding precipitation extremes

a. Introduction

1) DRY THEORETICAL EQUATORIAL WAVES

Equatorial waves have a robust theoretical foundation in meteorology (Wheeler and Nguyen 2025). They can be approximated as analytical solutions to the governing equations of atmospheric motion. Several key approximations are made in this theoretical framework (Matsuno 1966; Gill 1980):

- The background state is assumed to have zero motion, implying minimal or no vertical wind shear. However, this condition is rarely met in real-world tropical regions.
- The latitudinal variation of the Coriolis parameter is approximated as a linear function through the equatorial beta-plane approximation, expressed as $f = \beta y$. This approximation is generally reasonable.
- The wave solutions are assumed to be separable into vertical components (described by the vertical structure equation) and horizontal and temporal components (described by the shallow water equations).
- The amplitude of the waves is assumed to be small, meaning the waves are weak, allowing nonlinear advection terms to be neglected. However, this assumption does not hold for real equatorial waves observed in the atmosphere.
- Atmospheric motion is considered adiabatic, meaning that all diabatic heating, including radiative heating and latent heat release from condensation, is neglected. As a result, these theoretical wave solutions are often referred to as "dry" equatorial waves.

The purpose of outlining these approximations is not to provide a mathematical justification but to highlight that theoretical equatorial waves are idealized representations of real atmospheric phenomena. While these solutions offer valuable insights, real-world equatorial waves are influenced by complex atmospheric processes that may violate these idealized conditions.

Equatorial waves emerge as solutions to the simplified equations of atmospheric motion. Matsuno (1966) was the first to derive the free equatorial wave solutions, which serve as the fundamental "normal modes" of the tropical atmosphere. Much like the normal modes of vibration of a guitar string or drum, these equatorial wave normal modes create the music of the tropical atmosphere. Gill (1980) extended Matsuno's work by analyzing the forced equatorial wave response to latent heat release associated with mean tropical rainfall patterns. Gill's findings, encapsulated in the Matsuno–Gill model, explained many features of observed large-scale tropical circulation.

A useful way to visualize equatorial waves is through their dispersion relation (Fig. 1). This mathematical relationship connects the spatial scale of the waves, measured by their wavenumber k (where $k = 2\pi/\lambda$, with λ being the zonal wavelength) to their temporal scale, measured by their frequency ω (where $\omega = 2\pi/T$, with T being the waves' period). Only
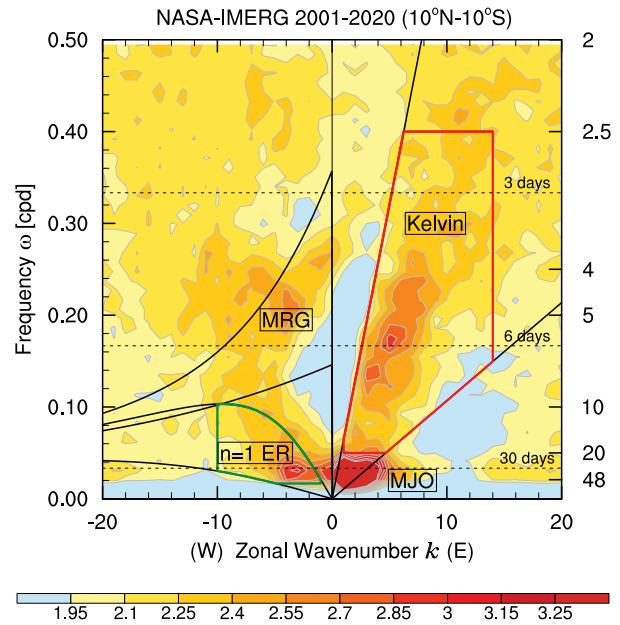

FIG. 1. Normalized wavenumber–frequency spectrum of daily precipitation data from GPM-IMERG (2001–20) superimposed with dispersion relation for equatorial waves. The spectrum is normalized by dividing the raw power by a smoothed background spectrum, obtained by averaging symmetric and antisymmetric components and then repeatedly smoothing the result with a 1–2–1 filter in both wavenumber and frequency. Superimposed are the theoretical dispersion curves of the odd meridional mode-numbered equatorial waves for the three equivalent depths of $h = 2.5$ and 90 m. The colored polygons indicate the region of wavenumber–frequency space used to filter for CCKWs and CCERWs. For MRG filtering, a broad bandpass (2–40-day periods and zonal wavenumbers 2–30) is applied, followed by projection onto its dynamical structures. See appendix B for further details on the spectral filtering configuration.

specific combinations of wavenumber and frequency are allowed, forming the characteristic dispersion curves in Fig. 1 (Wheeler and Nguyen 2025).

Different dispersion curves correspond to various types of equatorial waves, which are distinguished by their propagation direction (eastward or westward) and speed ($c = \omega/k$). The different types of waves also have very different spatial dynamical structures. The three primary types of equatorial waves, which will be the focus of this discussion, are

- equatorial Rossby waves,
- equatorial Kelvin waves, and
- mixed Rossby–gravity waves

These wave types play a significant role in atmospheric dynamics, contributing to large-scale weather patterns, accounting for 16%–20% of the total intraseasonal precipitation variance (Lubis and Jacobi 2015). Mathematical analyses and further details on the theoretical equatorial waves can be found in, e.g., Gill (1982). Equatorially trapped inertio-gravity waves are often subscale features within these three wave types and will also be discussed in section 2e.

The purpose of this review is to synthesize the growing body of literature that links equatorial waves to extreme precipitation. Extreme precipitation is considered in the context of hazardous rainfall with the potential to cause damage or pose risks to life. In the literature, equatorial-wave-driven rainfall is typically defined as extreme when the daily average at a grid point, over an area, or at a station, exceeds a high percentile threshold, often the 95th percentile. These thresholds are somewhat arbitrary, as lower rain rates can still be hazardous depending on factors such as floodplain extent, catchment conditions, and land management. Even so, percentile-based definitions are useful for identifying links between rainfall and larger-scale atmospheric processes. Ferrett et al. (2020) analyzed precipitation extremes across Southeast Asia (SEA) associated with Rossby, Kelvin, and mixed Rossby–gravity waves. They defined extreme precipitation as days when gridpoint rainfall exceeded the daily mean 95th percentile for 1998–2016 in a season. The corresponding threshold varied by location, but for context, this value averaged at around 40 mm day^{-1} in boreal winter and 25 mm day^{-1} in boreal summer over Indonesian landmasses (see Fig. 1 in Ferrett et al. 2020). Other studies cited in this review adopt slightly different thresholds, and readers should refer to each for precise definitions.

2) CONVECTIVELY COUPLED EQUATORIAL WAVES AND THEIR IDENTIFICATION METHODS

Among the various assumptions made in the derivation of theoretical equatorial waves, the most questionable one is arguably the assumption of dry adiabatic motion, with no tropical tropospheric diabatic heating associated with the waves. This assumption is problematic, particularly in the tropics, where latent heat release from deep moist convection is a crucial driver of tropical circulation. Other significant diabatic heat sources, such as radiation absorption and emission by clouds, surface heat fluxes in the boundary layer, and diabatic cooling from evaporation, are also overlooked. Given these omissions, it is remarkable that these simplified theoretical equatorial waves bear any relevance to real atmospheric conditions.

Since theoretical equatorial wave structures feature regions of convergence and divergence, as well as ascent and descent, it is highly likely that they interact strongly with moist convection, which is widespread across the tropics. This realization led to the concept of CCEWs (Gruber 1974; Wheeler et al. 2000), where observed wave structures in the real atmosphere exhibit similarities to the dry theoretical waves but are significantly modified by deep convection (Wheeler and Nguyen 2025). These waves include convectively coupled equatorial Rossby waves (CCERWs), convectively coupled Kelvin waves (CCKWs), and convectively coupled mixed Rossby–gravity (MRG) waves. A comprehensive review of these waves is provided by Kiladis et al. (2009).

There are two primary methods of identifying or diagnosing CCEWs, as described by Knippertz et al. (2022). The first method, known as wavenumber–frequency filtering, was introduced by Wheeler and Kiladis (1999) and is based on the rainfall signal associated with the waves, focusing on their convective component. To illustrate this process for CCKWs, observed precipitation data from the GPM-IMERG dataset are used. Initially, precipitation data are averaged meridionally across the equator (2.5°S–2.5°N) to create a longitude–time "Hovmöller" diagram (Fig. 2a). These longitude–time data are then transformed into wavenumber–frequency space using a two-dimensional Fourier transform.

A wavenumber–frequency diagram of daily precipitation data from GPM-IMERG is shown in Fig. 1, following the approach of Wheeler and Kiladis (1999). Dispersion curves for equatorial waves are superimposed on the spectrum, and a polygon is drawn around the region in wavenumber–frequency space corresponding to the wave type of interest. For instance, the red polygon in Fig. 1 encloses the equatorial Kelvin wave dispersion curve. This polygon serves as a filter: Data within it are retained, while those outside are set to zero. The filtered data are then subject to an inverse two-dimensional Fourier transform, converting them back to longitude–time space. The resulting filtered Hovmöller diagram displays only the precipitation features associated with CCKWs (Fig. 2b). CCKW trajectories, indicated by green lines in Fig. 2, are determined by tracking maxima in the filtered precipitation data. Further details on this method are available in Baranowski et al. (2016a) and Matthews (2021).

The wavenumber–frequency filtering method offers several advantages compared to a simple frequency (i.e., bandpass) filtering. It can discriminate between phenomena that operate in the same frequency range but have different spatial (wavenumber) characteristics, e.g., the CCKWs and MRG waves in Fig. 1. Since it is based directly on precipitation data or, alternatively, outgoing longwave radiation (OLR) (Huang and Huang 2011), a proxy for deep convection in the tropics, it captures the convective aspect of the waves without assuming any specific dynamical structure. Additionally, the extracted CCKW trajectories facilitate the development of an event- or object-based database. However, a notable limitation is that the Fourier transform and subsequent filtering may introduce difficulties in real-time monitoring and forecasting of CCEWs due to end effects, although these can be overcome (Janiga et al. 2018). Another constraint is that the input data are available on all longitudes.

Similar analyses can be conducted for other CCEWs by filtering different regions of wavenumber–frequency space. An additional refinement involves separately analyzing symmetric and antisymmetric components of the precipitation or OLR signal. Symmetric components (about the equator) are used for Kelvin and equatorial Rossby waves, whereas antisymmetric components are used for MRG waves. This separation enhances the accuracy of wave isolation.

The second method for diagnosing CCEWs involves projection onto theoretical dynamical wave structures, as described by Yang et al. (2003). This technique employs a dynamical field, such as the zonal or meridional wind at a specific vertical level. The field at each longitude is then projected onto the theoretical meridional structure of the relevant equatorial wave. One of the major advantages of this approach is that it does not assume the dispersion relation or vertical structure from theory (based on the theoretical assumption of a resting
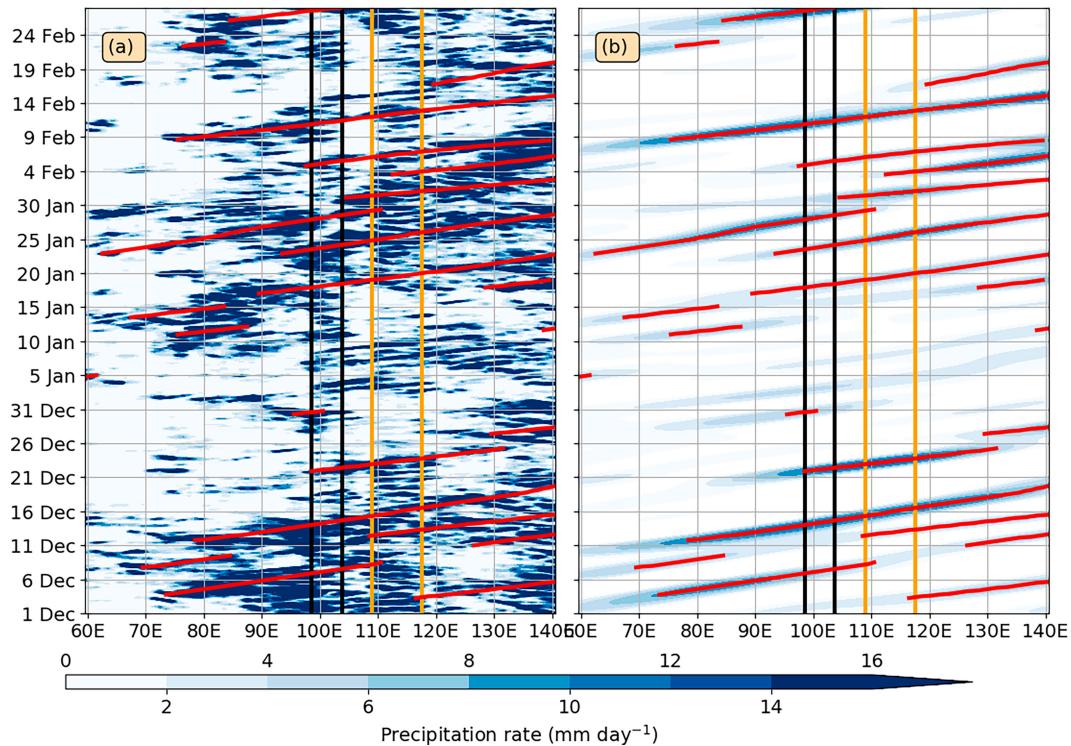
FIG. 2. Sample Hovmöller diagrams for equatorial (averaged 2.5°S–2.5°N) GPM-IMERGV07B precipitation for December 2022–February 2023: (a) unfiltered raw data and (b) CCKW filtered data. The red lines show the CCKW trajectories calculated from the filtered data. The two vertical black lines indicate the coastlines of Sumatra at the equator; the orange lines indicate Borneo.

basic state) and directly applies to observational data. These theoretical assumptions would otherwise be highly sensitive to background zonal flow variations with height and time, such as Doppler shift effects. Additionally, this method is well suited for real-time data monitoring. This method is also applicable for dry equatorial waves, which have no convective signal, unlike the wavenumber–frequency filtering method. However, this approach has certain disadvantages. It requires assumptions about the values of various theoretical wave parameters, and since analysis of waves identified using this method has typically been conducted at single longitudes and times, an event- or object-based database derived from this approach does not exist.

Several more recent techniques have been developed to isolate equatorial waves including spatial projection and 3D normal mode projection (e.g., Gehne and Kleeman 2012; Žagar et al. 2009), extended empirical orthogonal function (EOF) projection (e.g., Roundy 2012), and wavelet-based filtering (e.g., Kikuchi 2014). Knippertz et al. (2022) provide a detailed comparison of the advantages and disadvantages of the various methods and recommend users to try a range of methods to ascertain the robustness and reliability of any conclusions drawn.

b. CCERWs

1) HORIZONTAL STRUCTURE

This section introduces the westward-propagating CCERWs and examines their structure, focusing on the relationship between precipitation maxima and the associated wind and convergence patterns.

First, the horizontal structure of a theoretical equatorial Rossby wave during its passage over the MC is presented (Fig. 3). The wave exhibits symmetry about the equator. In this example, a pair of negative geopotential height anomalies (low pressure centers) is positioned on either side of the equator at the longitude of Borneo. The wind vectors indicate cyclonic circulation around each low pressure center (anticlockwise in the Northern Hemisphere and clockwise in the Southern Hemisphere) accompanied by westerly winds along the equator between them.

Conversely, regions to the west and east of these anomalies display opposite characteristics. At the longitudes of western Sumatra and New Guinea, positive geopotential height anomalies are present, with anticyclonic circulation (clockwise in the Northern Hemisphere and anticlockwise in the Southern Hemisphere) alongside easterly winds between them along the equator.

A region of convergence is present in the poleward flow to the east of the cyclonic circulations, near the longitudes of the Philippines and Darwin, Australia. If this structure represents the lower troposphere and the wave follows a "first internal mode" vertical structure, the spatial pattern in Fig. 3 would be mirrored in the upper troposphere with opposite signs. Therefore, upper-level off-equatorial divergence would occur at the longitudes of the Philippines and
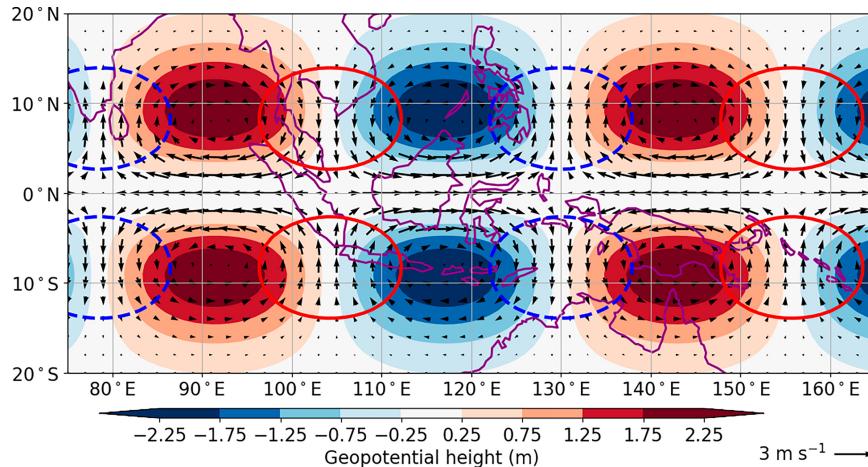
FIG. 3. Theoretical structure of $n = 1$ equatorial Rossby wave structure. Geopotential height anomalies are shaded (contour interval 0.5 m). Divergence anomalies are contoured, at -0.3×10^{-6} s^{-1} (blue dashed line) and 0.3×10^{-6} s^{-1} (red solid line). The standard wind vector has a magnitude of 3 m s^{-1}. Example given is for an equivalent depth of 15 m and zonal wavenumber 7. This structure can be interpreted as being representative of the lower-tropospheric structure of the equatorial wave at a suitable pressure level, e.g., 850 hPa. Note that the continental outlines are for information only on the scale of the waves; the theoretical wave structures are independent of any land–sea contrasts.

Darwin, leading to ascending motion in these regions due to mass conservation.

It is important to note that this theoretical equatorial Rossby wave is a dry wave, meaning it has no associated precipitation. However, if this wave structure were to interact with moist convection, precipitation would likely develop in the regions of poleward flow, low-level convergence (negative divergence), and ascent, i.e., in the regions within the blue dashed contours in Fig. 3.

Now, we examine the structure of observed CCERWs (Fig. 4). These are lagged composites derived from an event-based CCERW dataset, aligned with the crossing date of each CCERW trajectory passing the reference point at 120°E. The dataset was constructed using the wavenumber–frequency filtering method described in section 2, following Matthews (2025). The composite shows unfiltered IMERG precipitation anomalies, with only the seasonal cycle removed. This confirms that the CCERW structure is robust, not merely an artifact of wavenumber–frequency filtering, and strong enough to be detected in raw anomaly data, making it suitable for operational use.

The lag 0 composite map (Fig. 4b) reveals twin off-equatorial precipitation maxima near 115°E, one in the Northern Hemisphere over the South China Sea and a weaker one in the Southern Hemisphere, east of Java. These precipitation maxima align with the expected rainfall distribution of a theoretical equatorial Rossby wave. The sequence of lagged composites from lag −2 days (Fig. 4a) to lag +4 days (Fig. 4d) clearly illustrates westward propagation, with an estimated phase speed of 4 m s^{-1}.

The precipitation anomalies are noticeably influenced by the underlying land–sea distribution of the MC (Matthews 2025). For instance, they are particularly strong, exceeding 4.5 mm day^{-1}, over the Philippines (Fig. 4a) and South China Sea (Figs. 4b,c), but weaken significantly upon reaching Vietnam and mainland Southeast Asia (Figs. 4c,d). The lower-tropospheric dynamical structure of the CCERW (Fig. 4) closely resembles the theoretical structure in Fig. 3, particularly in the arrangement of the cyclone/anticyclone pairs and the zonal and meridional wind patterns. However, a key difference lies in the position of the convergence regions. In the CCERW (Fig. 4), these regions align with the cyclonic structures at the same longitude, whereas in the theoretical equatorial Rossby wave (Fig. 3), they are shifted a quarter wavelength to the east. Additionally, the precipitation anomalies in the CCERW (Fig. 4) coincide with the convergence anomalies, marking a significant departure from what would be expected based on the theoretical wave structure. The reason for this is unclear. Potential mechanisms could involve scale interactions, with mesoscale convective systems developing within the envelope of CCERW cyclonic vorticity. Their resulting overturning circulation could lead to low-level convergence, which feeds back onto the large-scale CCERW structure. This is an area of current research.

The dynamical structure at 850 hPa (Fig. 4) is approximately repeated at all levels in the lower troposphere (Matthews 2025), consistent with the theoretical wave. However, in the upper troposphere, it changes character, being dominated by a strongly divergent wind structure with much weaker vorticity centers. This is in contrast to the vertical modal structure (a pattern of one sign at the low level replaced by the same pattern but with the opposite sign at the upper level) of the theoretical equatorial Rossby wave. Hence, these commonalities and differences support the assumption
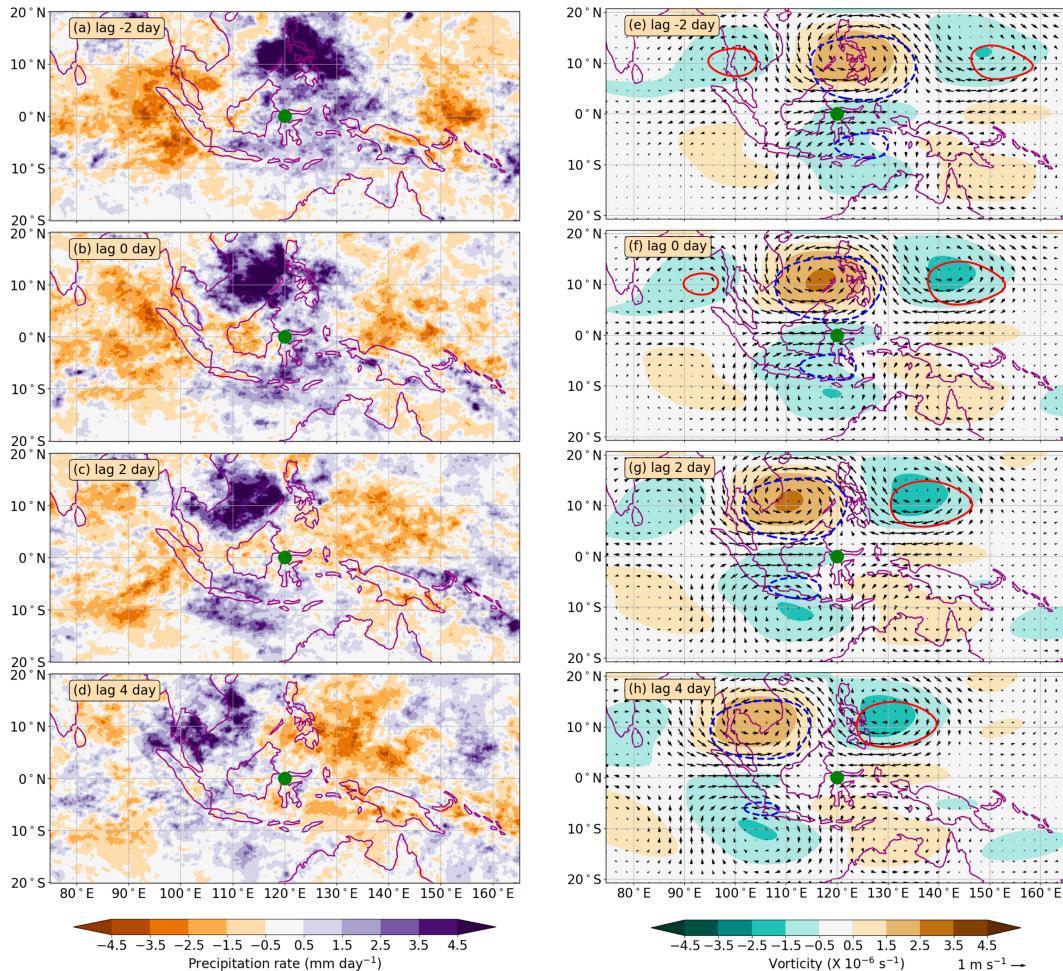
FIG. 4. Lagged composite of unfiltered GPM-IMERG precipitation anomalies for a CCERW at lag (a) −2, (b) 0, (c) +2, and (d) +4 days. Lags are relative to the crossing time at the base point at 120°E shown by the green circle. Composites were calculated from year-round data from 2000 to 2023 and are the average of approximately 300 individual events. (e)–(h) As in (a)–(d), but for the ERA-Interim 850-hPa dynamical structure of the CCERW. Anomalies are wavenumber–frequency filtered. Vorticity anomalies are color shaded (interval 1×10^{-6} s^{-1}). Divergence anomalies are contoured at -0.25×10^{-6} s^{-1} (blue dotted line) and $+0.25 \times 10^{-6}$ s^{-1} (red solid line). Standard wind vector is 1 m s^{-1}.

that a CCERW can be understood as a theoretical equatorial Rossby wave modified by the effects of moist convection.

CCERWs can be monitored in real time using both the wavenumber–frequency method (Wheeler and Weickmann 2001) and the dynamical structure method (Yang et al. 2021). Since the spatial relationship between precipitation and the dynamical structure of CCERWs is well understood, tracking and predicting CCERW structures can offer valuable insights for forecasters in anticipating CCERW-associated precipitation, as will be shown in the following subsection.

2) CCERWs AND EXTREME PRECIPITATION

Several studies have identified connections between CCERWs and extreme precipitation events. Typically, regions experiencing extreme precipitation coincide with the passage of a CCERW, leading to enhanced convection.

For example, during the December–February season, the probability of extreme precipitation over eastern Peninsular Malaysia increases threefold at the center of the cyclonic anomaly. A similar increase in extreme precipitation probability has been observed over the Philippines during the passage of high-amplitude CCERWs (Ferrett et al. 2020). Evidence also shows that the convectively active phases of CCERWs amplify the likelihood of extreme rainfall events over Java, Indonesia, by up to 45% relative to the total probability during wintertime (Lubis and Respati 2021).

CCERWs can also interact nonlinearly with other convectively coupled waves and tropical systems. Over Sulawesi, the probability of extreme precipitation or flooding nearly doubles when either a CCERW or a CCKW passes through (Latos et al. 2021). However, when both waves occur simultaneously, the probability increases eightfold. The influence of CCERWs
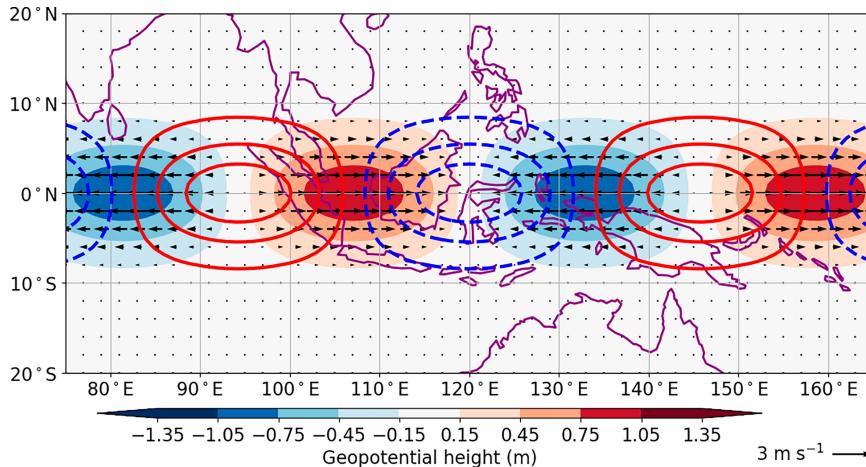
FIG. 5. Theoretical structure of equatorial Kelvin wave. Geopotential height anomalies are shaded (contour interval 0.3 m). Divergence anomalies are line contoured, with an interval of 0.6×10^{-6} s^{-1}. Positive contours are shown by red solid lines; the first positive contour is at 0.3×10^{-6} s^{-1}. Negative contours are shown by blue dashed lines; first negative contour is at -0.3×10^{-6} s^{-1}. The standard wind vector has a magnitude of 3 m s^{-1}. Example given is for a phase speed of 6 m s^{-1} and zonal wavenumber 7. This structure can be interpreted as being representative of the lower-tropospheric structure of the equatorial wave at a suitable pressure level, e.g., 850 hPa. Note that the continental outlines are for information only on the scale of the waves; the theoretical wave structures are independent of any land–sea contrasts.

and CCKWs was particularly significant in triggering the Makassar flood on 22 January 2019, the largest recorded flood in the region.

In addition to directly increasing the likelihood of extreme precipitation through enhanced rainfall at the center of the CCERW cyclonic anomaly, CCERWs can also contribute indirectly. For instance, during the development of Tropical Cyclone Seroja in the MC, a CCERW acted as a moisture supplier, advecting moisture around its cyclonic circulation to fuel the developing cyclone (Latos et al. 2023). The tropical cyclone's convection was then further intensified by the cyclonic vorticity within the CCERW. Additionally, CCERWs have been linked to cold surges on the western flank of their cyclonic anomalies over the South China Sea, which can trigger extreme precipitation in the region (Diong et al. 2023).

More broadly, CCERWs frequently influence tropical cyclones. Over the western North Pacific, they serve as precursors to 44% of pretropical cyclogenesis events (Feng et al. 2023). When tropical cyclones align with CCERWs, their intensification rate increases. CCERWs can also impact the strength of the monsoon circulation (Pramuwardani et al. 2018).

c. CCKW

1) HORIZONTAL STRUCTURE

Equatorial Kelvin waves are special solutions of the shallow water equations in which the meridional wind component vanishes. Unlike other classes of equatorial waves, Kelvin waves follow a simple linear dispersion relation: All wavelengths propagate eastward with the same phase speed, making them nondispersive (red line, Fig. 1). Their structure is

symmetric about the equator, with amplitudes of pressure, zonal wind, and divergence maximizing at the equator and decaying with latitude (Fig. 5). Along the equator, Kelvin waves are characterized by alternating regions of low and high pressure, westerly and easterly winds, and convergence and divergence. Convergence occurs where westerly anomalies to the west meet easterly anomalies to the east, as illustrated here over the Maritime Continent (Fig. 5). When Kelvin waves are convectively coupled, rainfall intensifies in the convergent phase, where rising motion and moisture convergence favor deep convection. In contrast, the divergent phase suppresses convection, leading to reduced rainfall.

CCKWs feature many similarities to the dry theoretical solutions. In Fig. 6, we examine lagged composites of the Kelvin wave–filtered zonal winds, divergence, and vorticity at 850 hPa. These composites are calculated based on the time when a CCKW, such as those presented in Fig. 2, crosses a base point of 120°E. The composite 850-hPa wind structure (Fig. 6) is similar to that of the theoretical structure (Fig. 5), exhibiting a pattern of alternating westerlies and easterlies along the equator. There is a weak meridional wind component that arises as the flow is only approximately geostrophic. A region of convergence centered on the Karimata Strait on lag day -2 is flanked by the westerly anomalies to the west and the easterly anomalies to the east and has progressed over the west Pacific Ocean (north of New Guinea) by lag day 1 (Fig. 6). CCKWs are known to cover a longitudinal distance of around 10° over the course of a day, corresponding to a phase speed of about 10–15 m s^{-1} (Kiladis et al. 2009). This is evident in the composite structure, in which the center of convergence is located approximately 10° further east between each lag day. The composite 850-hPa vorticity structures (Fig. 6) are similar to
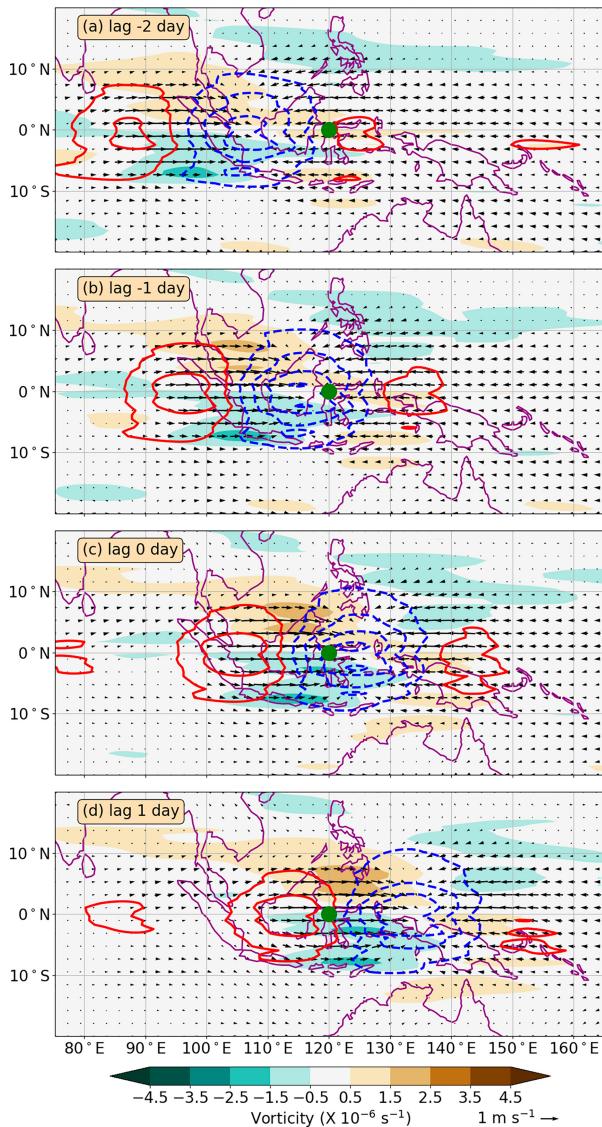
FIG. 6. Lagged composites of the ERA-Interim 850-hPa dynamical structure of the CCKW at lag (a) −2, (b) −1, (c) 0, and (d) 1 days. Lags are relative to the crossing time at the base point at 120°E shown by the green circle. Anomalies are wavenumber–frequency filtered. Vorticity anomalies are color shaded (interval 1×10^{-6} s^{-1}). Divergence anomalies are line contoured, with an interval of 0.6×10^{-6} s^{-1}. Positive contours are shown by red solid lines; the first positive contour is at 0.3×10^{-6} s^{-1}. Negative contours are shown by blue dashed lines; first negative contour is at -0.3×10^{-6} s^{-1}. The standard wind vector is 1 m s^{-1}.

the theoretical structure (Fig. 1 of Matthews 2021), where a dipole of cyclonic shear is collocated with the westerly anomaly. However, the dipole of anticyclonic shear in the composite is weaker compared to the theoretical structure.

While the dynamical structure of zonal wind and divergence of CCKWs are broadly similar to the dry waves, the phasing between the zonal wind anomalies and geopotential height may differ (Roundy 2012). Their propagation and growth mechanisms are also more complex than those of their

dry counterparts (Matthews 2021). As with other equatorial waves, the observed vertical structure is similar at each level to the dry theoretical structure. However, the pattern shifts increasingly westward with height over most of the troposphere up to about 400 hPa (Kiladis et al. 2009).

Lagged composites of raw, unfiltered precipitation anomalies based on the times when a CCKW crosses a base point of 120°E (Fig. 7) show remarkable correspondence to the filtered dynamical structures (Fig. 6). A region of eastward-propagating anomalous precipitation crosses the base point at 120°E on lag day 0. Regions of enhanced precipitation coincide with the regions of Kelvin wave convergence and vice versa (Fig. 6). This confirms that these dynamical structures correspond to Kelvin waves rather than an artifact of filtering.

As with CCERWs, CCKWs are influenced by the land–sea distributions over the MC with greater precipitation anomalies over the seas compared to land. On lag −2 days (Fig. 7a), there is a clear reduction in precipitation over the west coast of Sumatra. The Barisan Mountains are aligned along the west coast of Sumatra, which act as a barrier to incoming CCKWs. This often results in a component of the CCKW being deflected by the barrier and becoming topographically trapped, traveling parallel to the mountain range (Fine et al. 2016).

2) CCKWs AND EXTREME PRECIPITATION

Numerous studies have linked CCKWs to precipitation extremes across the MC (van der Linden et al. 2016; Ferrett et al. 2020; Baranowski et al. 2020; Lubis and Respati 2021; Latos et al. 2021; Senior et al. 2023, 2025). The amplitude of the convergent phase of a CCKW usually maximizes over the equator and is associated with enhanced precipitation. The convergent phase of a CCKW increases the likelihood of extreme precipitation by a factor of 2–4 over the near-equatorial regions of the MC (Ferrett et al. 2020). For example, Lubis and Respati (2021) reported that the convectively active phases of Kelvin waves increase the occurrence of extreme rainfall events over Java, Indonesia, by up to 60% relative to the climatological probability of extreme precipitation during the winter season. Due to its location as the first major island in the path of an incoming CCKW and its unique topography, Sumatra is particularly vulnerable to rainfall extremes caused by eastward-propagating weather systems. In an innovative study incorporating social media reports as well as government reports (Baranowski et al. 2020), it was found that 90% of floods in Sumatra were attributed to the presence of CCKWs between 2014 and 2018.

The link between CCKWs and rainfall extremes over the MC is known; however, the mechanisms through which CCKWs influence these extremes are less understood. CCKWs move through a particular longitude over the course of a day or two, which may result in them interacting strongly with the diurnal cycle of rainfall. On the west coast of Sumatra, this is comprised of an afternoon peak over the Barisan Mountains, which propagates to the west coast in the evening, peaking there at around 1500 UTC, before propagating offshore overnight with the land breeze (Bai et al. 2021; Peatman et al. 2023). Baranowski et al. (2016b) found that CCKWs arriving
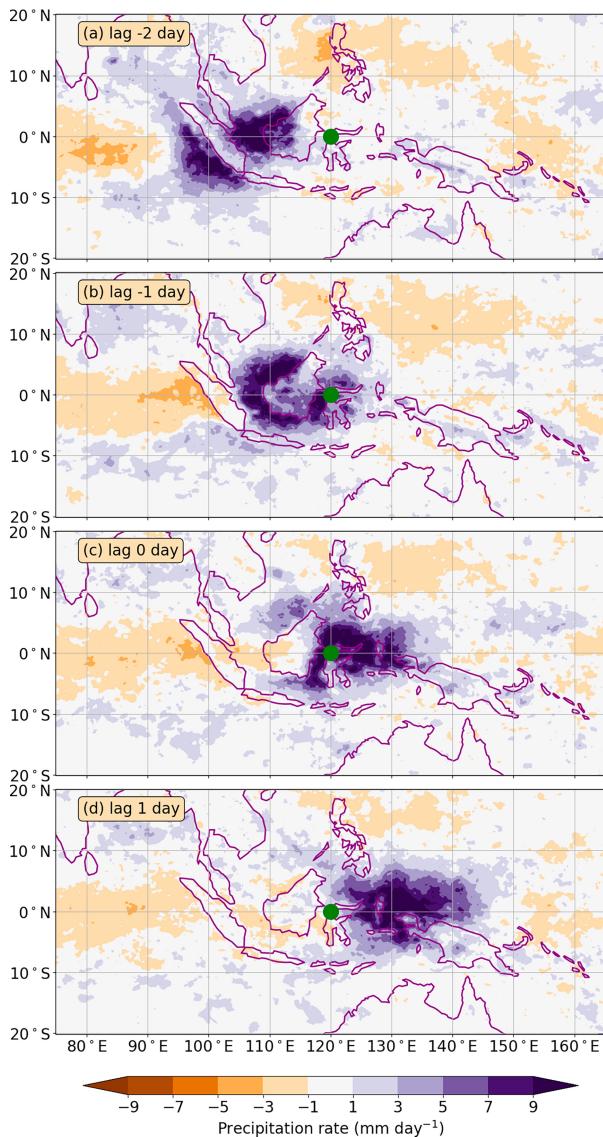
FIG. 7. As in Fig. 6, but for unfiltered GPM-IMERG precipitation anomalies.

event. Nguyen et al. (2025) also evidenced the crucial role of CCKWs in the initialization and eastward propagation of the squalls over Sumatra and the Strait of Malacca, often leading to strong winds and heavy rainfall causing important damage to infrastructure. Baranowski et al. (2016b) also found that CCKWs that arrive in phase with the diurnal cycle in Sumatra are more likely to traverse the MC. Since Borneo is positioned roughly 10° east of Sumatra, CCKWs coincidentally are able to travel the distance of one island over the course of 1 day. This means that CCKWs arriving in time with the diurnal cycle of Sumatra are likely to also arrive in time with the diurnal cycle of Borneo and be given several diurnal "boosts."

CCKWs can also exist independently, and they are a major subscale feature of the active MJO envelope, described by Kikuchi et al. (2018) as its "building blocks." CCKWs tend to travel slower when embedded in an active MJO envelope (Roundy 2008). The MJO itself has also been linked to precipitation extremes over the MC (Da Silva and Matthews 2021) and intensification of the diurnal cycle (Peatman et al. 2014). When part of a multiscale interaction with the MJO, CCKWs can be associated with devastating precipitation extremes (Latos et al. 2021; Saufina et al. 2025; Senior et al. 2025). CCKWs were found to be present in all MJO-related floods in Sumatra (Baranowski et al. 2020), suggesting that CCKWs are primary predictors of MJO-related precipitation extremes, organizing convection at a more localized scale. Senior et al. (2025) examined a case study in July 2021, where scale interactions between CCKWs, the MJO, and diurnal boosts provided ideal conditions for a CCKW to traverse the MC, triggering intense precipitation over a large area and causing a local termination of the active MJO event.

d. MRG wave

1) HORIZONTAL STRUCTURE

Since its discovery by Yanai and Maruyama (1966), the $n = 0$ westward-moving equatorial wave has emerged as one of the significant tropical waves. To date, it has been investigated for its influence and its association with other atmospheric phenomena. However, this wave type is not yet fully understood; Kiladis et al. (2016) and Dias and Kiladis (2016) note that there are still inconsistencies between the observed behavior of the MRG wave and theory. According to Matsuno's (1966) wave solution, the equatorial waves moving westward with $n = 0$ exhibit a combination of equatorial Rossby wave and westward-propagating gravity wave characteristics.

It is important to note that theoretically there exist eastward-moving MRG waves. Here, we focus only on westward-moving MRG waves. The primary reason for this is that very few studies have examined this wave type in detail in relation to rainfall over the MC, as pointed out in Kiladis et al. (2016). This is perhaps because of its generally higher frequency or potentially lower amplitude, which may make them more difficult to identify (Yang and Hoskins 2016; Kiladis et al. 2016). The role of this wave type on rainfall over the MC should certainly be a focus of future research. However, for the remainder of this article, MRG waves will be referred to as the westward-moving MRG wave only.

at Sumatra in phase with the convection associated with the local diurnal cycle of the west coast of Sumatra had greater precipitation amplitudes. Senior et al. (2023) found that CCKWs linked to precipitation extremes in the city of Padang on the west coast of Sumatra would modulate the local diurnal cycle of rainfall. The additional low-level moisture and convergence provided by the CCKW intensified the nocturnal offshore propagating component of diurnal convection; then, the combined convergence line of both systems is displaced toward the coast over the course of the night. Different from the typical diurnal cycle, this resulted in an increase in coastal rainfall overnight and over the following day. Similarly, Lopez-Bravo et al. (2023) found that Kelvin wave activity propagating along the eastern Indian Ocean may prolong the life of diurnally driven squall lines over Sumatra, which may lead to an extreme rainfall
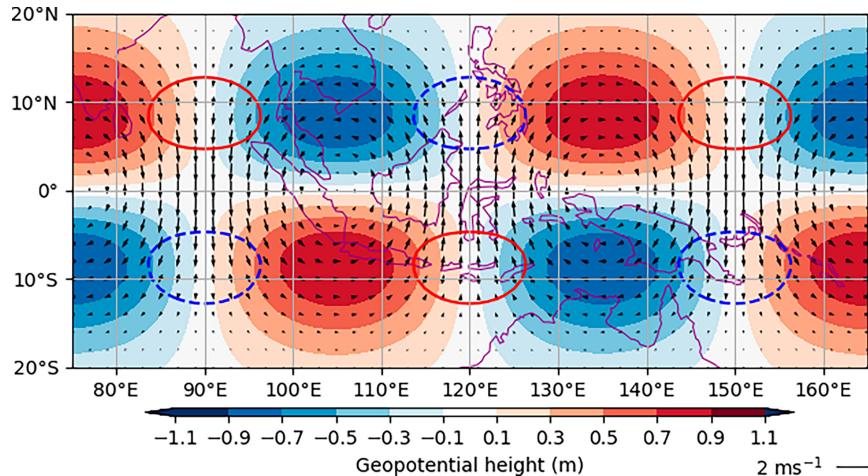
FIG. 8. Theoretical structure of MRG wave. Geopotential height anomalies are shaded (contour interval 0.2 m). Divergence anomalies are line contoured, with an interval of $0.4 \times 10^{-6}\,\mathrm{s}^{-1}$. Positive contours are shown by red solid lines; the first positive contour is at $0.2 \times 10^{-6}\,\mathrm{s}^{-1}$. Negative contours are shown by blue dashed lines; first negative contour is at $-0.2 \times 10^{-6}\,\mathrm{s}^{-1}$. The standard wind vector has a magnitude of 2 m s^{-1}. Example given is for zonal wavenumber 6. Note that the continental outlines are for information only on the scale of the waves; the theoretical wave structures are independent of any land–sea contrasts.

The theoretical structure of MRG waves consists of alternating clockwise and anticlockwise circulation centered on the equator, resulting in easterly and westerly winds off the equator and meridional winds crossing the equator. Figure 8 shows the asymmetric nature of the structure of the MRG wave. The wave structure has convergence (or divergence) in the Northern Hemisphere coinciding with opposing divergence (or convergence) in the Southern Hemisphere, as a result of the circulation centered on the equator. Figure 9 shows lagged composites of unfiltered precipitation anomalies (colored shading) and filtered and projected MRG wave 850-hPa horizontal winds (vectors) and associated convergence and divergence (line contours) for MRG waves crossing Peninsular Malaysia. In this instance, MRG waves have been identified at 850 hPa in ERA5 reanalysis using the Yang et al. (2003) method, where zonal winds, meridional winds, and geopotential height are filtered temporally and spatially and then projected onto theoretical wave structures. Composites are calculated with reference to the Northern Hemisphere convergence (at 8°N) associated with the MRG wave crossing a longitude band over Peninsular Malaysia (100°–105°E). The choice of latitude is based on the theoretical structure of the wave used for projection, where the peak of convergence and divergence occurs around 8°N and 8°S. The longitude range was chosen to produce a smoother signal of dynamical wave activity, compared to a single point, and was chosen to roughly span Peninsular Malaysia.

Figure 9 shows that increased precipitation occurs in regions of MRG wave convergence. At lag −2 days, as the MRG waves approach Vietnam, there are positive precipitation anomalies just off the east coast of Vietnam, coinciding with the peak of MRG convergence. Similarly, over the Indian Ocean off the southwest coast of Sumatra, positive precipitation

anomalies along with MRG convergence in the Southern Hemisphere are observed. The drying in the Northern Hemisphere to the west of Peninsular Malaysia, coincident with MRG divergence, is also evident. As with the CCERW, the impact of the land–sea distribution on the precipitation anomalies in this region is clear, with larger increases in rainfall over the ocean and on the east coast compared with over land. Similarly, rainfall anomalies tend to be larger in the Northern Hemisphere than in the Southern Hemisphere. As the MRG waves propagate westward, at lag −1 days, rainfall increases on the east coast of Vietnam where Northern Hemisphere MRG convergence occurs over land. When the MRG wave convergence reaches Peninsular Malaysia at lag 0 days, these enhanced rainfall anomalies are observed in the north and along the east coast of Peninsular Malaysia. These anomalies are still evident at lag +1 days due to the persisting convergence from the MRG wave over the region. As with the observed Rossby waves, convergence aligns more closely with the cyclonic structures in the wave, as opposed to the theoretical wave structure where convergence is strongest where meridional winds converge, between the regions of vorticity.

2) MRG AND EXTREME PRECIPITATION

Kiladis et al. (2009) found that MRG waves predominantly occur in the central and western Pacific regions. This confirms results from an earlier study by Hendon and Liebmann (1991) that suggested that MRG waves occur predominantly in the central Pacific due to the unique meridional SST gradients there. Areas with off-equatorial poleward flow indicate heightened convection, while equatorward flow signals suppressed convection (Kiladis et al. 2009). This poleward flow, associated with displaced heating in off-equatorial gyres, plays a significant role in tropical cyclogenesis (Itoh and Ghil 1988;
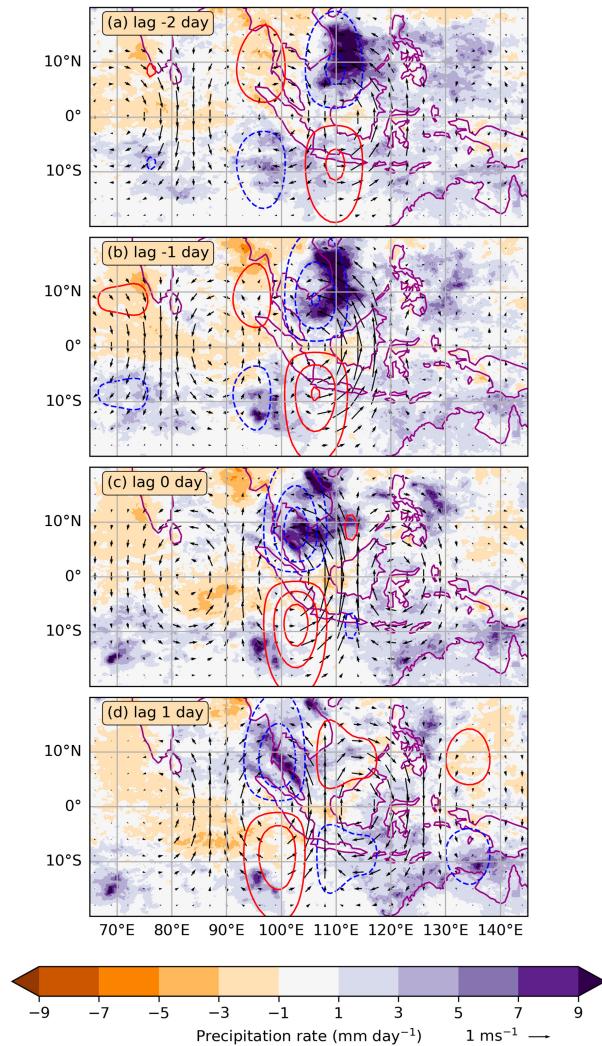
FIG. 9. Lagged composite of unfiltered GPM-IMERG daily precipitation anomalies for Northern Hemisphere convergence associated with a westward-moving MRG wave at lag (a) −2, (b) −1, (c) 0, and (d) 1 days. In these cases, MRG waves are identified dynamically using the method of Yang et al. (2003). Vectors show dynamically filtered standardized ERA5 MRG 850-hPa horizontal wind. Line contours show the corresponding horizontal wind convergence (dashed blue) and divergence (solid red). Line contours are at intervals of 1 std dev starting at 0.5. Lags are relative to strong MRG convergence (>2 std dev) at 8°N and 100°–105°E. Composites are calculated from year-round data for 2001–22 and are the average of 207 events.

Zhou and Wang 2007; Chen and Huang 2009; Feng et al. 2023).

The link between MRG and precipitation in the MC is evidenced in Fig. 9. Several studies have demonstrated the influence of MRG waves on weather patterns in the MC. A recent study by Hu et al. (2023) revealed that MRG waves can contribute to triggering the South China Sea summer monsoon (SCSSM) onset, as evidenced in 2023. Additional studies underscore the impact of MRG waves on rainfall in Southeast

Asia. Ferrett et al. (2020) find that MRG waves are linked to increased rainfall in several regions of Southeast Asia, including Peninsular Malaysia, Java, and the Philippines. They find that extreme rainfall can be 3–4 times more likely in some regions because of MRG wave activity. Lubis and Respati (2021) also find that extreme rain events in Java are increased by 40% because of convectively active MRG waves.

Crook et al. (2024) suggest that most of the rainfall associated with MRG waves in Southeast Asia is related to tropical cyclones. Geng and Katsumata (2021) emphasize that MRG waves contribute to diurnal phenomena on both regional and local scales, especially over the southwestern coast of Sumatra Island. Although MRG waves are generally recognized as precursors to tropical cyclone genesis in the western Pacific (Itoh and Ghil 1988; Zhou and Wang 2007; Chen and Huang 2009), insights from Schreck et al. (2011) have clarified the transition into a tropical depression (TD)-type disturbance process.

e. Inertio-gravity waves

Equatorial inertio-gravity (IG) waves come in several forms. The most familiar are the equatorially trapped modes, which occur for higher meridional mode numbers ($n \geq 1$). These include both westward-propagating IG (WIG) and eastward-propagating IG (EIG) branches of wavenumber–frequency spectra (see, e.g., Fig. 1 in Wheeler and Kiladis 1999). The $n = 1$ WIGs are particularly energetic and commonly associated with convective disturbances lasting 1–3 days, with phase speeds of 10–30 m s^{-1} (Wheeler and Kiladis 1999; Kiladis et al. 2009). EIGs with $n \geq 1$ are observed less frequently and contribute less power to the spectra. However, their role in producing precipitation extremes should not be understated.

There are also special solutions associated with the lowest meridional mode ($n = 0$). One of these is the MRG wave that has been discussed in section 2d, which always propagates westward but changes its character with scale: At long wavelengths, it behaves more like a Rossby wave, while at shorter wavelengths, it takes on the properties of an IG wave. Another $n = 0$ solution is the so-called EIG continuum. In wavenumber–frequency spectra of tropical convection (see Fig. 1 in Wheeler and Kiladis 1999), there is clear evidence for eastward-propagating variance at periods of a few days that aligns with the theoretical $n = 0$ EIG dispersion curves (Wheeler and Kiladis 1999; Kiladis et al. 2009). However, these waves are not equatorially trapped, lacking the sharp meridional confinement that makes other equatorial modes easier to isolate and study. It is also worth noting that the $n = 0$ MRG and $n = 0$ EIG continuum are not always easy to separate in practice: Both project onto convective variability at periods of 2–5 days, but while the MRG appears as a discrete, antisymmetric mode, the EIG branch is spectrally more diffuse, making it less distinct in observations (Wheeler and Kiladis 1999; Kiladis et al. 2009, 2016; Dias and Kiladis 2016). As a result, although their spectral signature is strong, their physical role in organizing convection and rainfall remains less well understood, and they have received comparatively little attention in the literature (Kiladis et al. 2016; Dias and Kiladis 2016).

A distinction exists between IG waves and diurnal gravity waves, and the latter are often excited by afternoon island convection in the MC, while the former emerge as normal modes of the Matsuno–Gill model (Matsuno 1966; Gill 1980). Yet, the two are connected: Diurnal gravity waves can act as a forcing mechanism that excites equatorial IG waves. Because of this, some IG modes, in particular the westward $n = 1$ WIG modes, so-called 2-day waves, demonstrate strong diurnal phase locking (Nakazawa 1988; Takayabu 1994; Chen et al. 1996; Liebmann et al. 1997; Ruppert and Zhang 2019).

In the MC, satellite and reanalysis studies show that IG modes are commonly embedded within the broader tropical convective spectrum (Nakazawa 1988; Kiladis et al. 2009). Observations during the DYNAMO field campaign in the central Indian Ocean (2011–12) revealed how convection routinely excites IG waves with periods of 1–3 days within the MJO envelope (Yu et al. 2018). Kikuchi et al. (2018) described how during a particular MJO event in the campaign, $n = 1$ WIGs, along with CCKWs, were a ubiquitous subscale feature of the large-scale convective envelope. Senior et al. (2025) analyzed a case in July 2021, during which CCKWs embedded in an active MJO interacted with $n = 1$ WIGs that were phase locked to the diurnal cycle over the MC. The WIGs helped sustain the final CCKW as it moved across Sumatra, Borneo, and Sulawesi, where the combined wave activity produced heavy rainfall, leading to widespread reports of flooding and landslides. The magnitude of the precipitation was sufficient to alter the large-scale atmospheric state, drying out the water column and triggering an abrupt termination of the MJO event. This case study demonstrates how IG waves can influence both local extremes and the evolution of large-scale modes, linking diurnal convection with synoptic- and planetary-scale variability.

Despite their prevalence and fundamental role in the hierarchical structure of tropical convection, IG waves have been underrepresented in the literature compared to other equatorial modes. This is because their fast time scales, small spatial scales, and tendency to be embedded in larger-scale convective systems make them hard to isolate in observations and models. However, field campaigns such as DYNAMO, high-resolution reanalyses and convective-scale models, and improved satellite datasets are offering new opportunities to study the role of IGs in producing precipitation extremes.

3. Current state of equatorial wave forecasting and associated precipitation extremes in the MC

a. Challenges and approaches in forecasting equatorial waves and extreme precipitation in the Maritime Continent

The ability of numerical weather models to accurately forecast equatorial waves is crucial for predicting extreme weather events, such as heavy rainfall and tropical cyclones. Despite the fact that equatorial waves have been the subject of global forecasting and monitoring for many years (Wheeler and Weickmann 2001; Molinari et al. 2006), their incorporation into numerical forecast models for the MC remains challenging. This section

reviews recent progress and ongoing challenges in forecasting equatorial waves and their associated impact on extreme weather for the MC.

Over the last two decades, climate and forecast models struggled to represent most modes of CCEW variability (e.g., Lin et al. 2006; Kiladis et al. 2009; Straub et al. 2010; Hung et al. 2013; Dias et al. 2018; Schreck et al. 2020). This challenge is primarily due to the poor performance of numerical models in capturing tropospheric convection–circulation coupling, which relies on accurate representations of subgrid-scale processes such as cloud microphysics, boundary layer dynamics, precipitation, and radiation.

However, recent studies indicate significant improvements in the representation of equatorial waves at longer lead times by operational forecast models, particularly on the S2S time scale (Janiga et al. 2018; Dias et al. 2023). For example, using the European Centre for Medium-Range Weather Forecasts (ECMWF) forecast system, Dias et al. (2023) showed that the forecast skill of CCEWs can be improved when the operational forecast models are initialized with minimal bias in the basic state and anomalous tropical forcing. This is consistent with Janiga et al. (2018), who showed that biases in the mean state and the activity of the MJO and CCEWs are smaller in the ECMWF model than in other medium-range weather forecast models.

Despite this improvement, the predicted tropical subseasonal variability associated with the waves, such as precipitation, remains underestimated (see Fig. 4 in Dias et al. 2023). This underestimation is attributed to biases in the amplitude and propagation speeds of CCEWs in the operational forecast model, which reduce the accuracy of precipitation forecasts (e.g., Dias et al. 2018; Janiga et al. 2018; Dias et al. 2023). The cause of equatorial wave biases in models remains unclear; possible factors include incorrect coupling between convective and dynamical processes (Dias et al. 2018, 2023; Yang et al. 2021), biases in the background flow (Yang et al. 2021, 2023), and biases in the representation of interannual variability (Yang et al. 2023). The cause of equatorial wave bias is likely a combination of factors. These are discussed in more detail in section 4a.

Accurately forecasting wave-related high-impact weather in the MC also remains challenging. Recent studies have suggested methods that leverage the statistical relationship between equatorial waves and heavy rainfall to forecast heavy rainfall in the MC (Ferrett et al. 2023; Wolf et al. 2024). These methods, known as "hybrid dynamical–statistical forecasts," create probabilistic rainfall forecasts by combining NWP forecasts of the dynamical fields associated with equatorial waves and the observed relationship between heavy rainfall and these waves (Ferrett et al. 2023; Wolf et al. 2024). The skill of these hybrid forecasts varies with time of year and location and depends on the accuracy of wave activity forecasts and the observed relationship between equatorial waves and heavy rainfall. These studies offer potential improvement in forecasting high-impact weather if equatorial wave information is directly incorporated. They also confirm that the accuracy of heavy rainfall forecasts is limited by the precision of equatorial wave activity in models, as highlighted by Dias et al. (2023). While the
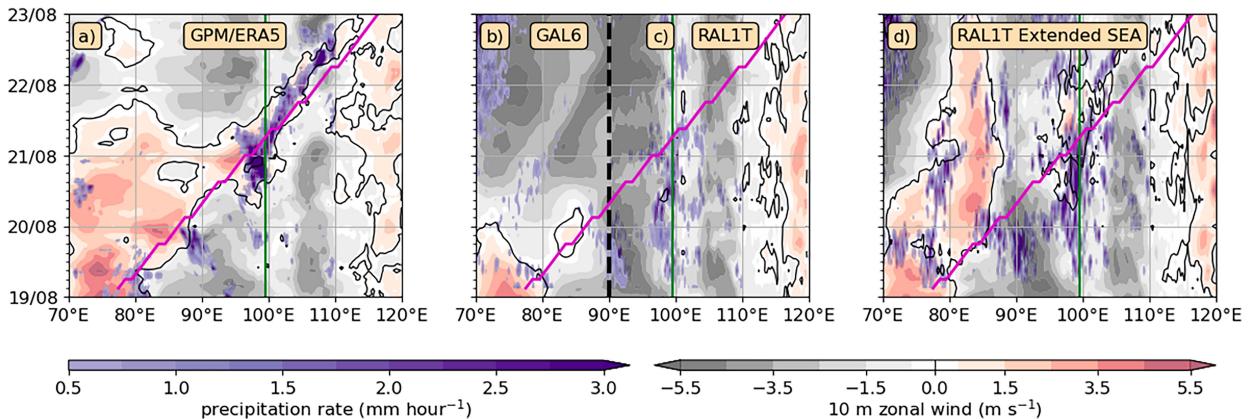
FIG. 10. Comparison of MetUM CP forecasts with different domain extents of an extreme precipitation event in Padang, Sumatra, on 21 Aug 2017 based on work in Senior et al. (2023). Hovmöller diagram of precipitation rate (purple shading) and 10-m zonal winds (gray–red shading) as represented by (a) GPM-IMERG (precipitation) and ERA5 (zonal winds), (b) the GAL6 11-km parameterized convection forecast, (c) the RAL1T 4.4-km SEA explicit convection forecast, and (d) the RAL1T 4.4-km explicit convection forecast on an extended SEA domain. All models presented here are initialized at 0000 UTC 19 Aug 2017. The SEA domain spans 18°S–30°N, 90°–154°E, and the extended SEA domain extends the western boundary to 65°E. The GAL6 global model drives the RAL1T nested models. The western boundary between the GAL6 global model in (b) and the nested RAL1T model in (c) at 90°E is marked by the black dotted line in the middle panel. The green line marks the longitude of Padang on the west coast of Sumatra. The observed CCKW trajectory, as calculated using wavenumber–frequency filtering of IMERG rainfall (Matthews 2021), is shown in magenta.

system combining hybrid forecasts with NWP forecasts is still in its earlier stage, it provides a pathway for advancing the prediction of CCEW-associated extreme precipitation.

The sensitivity and predictability of a wave-induced extreme rainfall event in the MC have also been studied by Doyle et al. (2023) and Senior et al. (2023). By utilizing the U.S. Navy's Coupled Ocean–Atmosphere Mesoscale Prediction System (COAMPS) forecast, Doyle et al. (2023) demonstrated the utility of adjoint-based perturbation methods, which use an "adjoint" model (e.g., Doyle et al. 2012, 2014) to identify how small, targeted changes in the initial state affect forecast parameters at a later state. They pinpointed critical components and interactions between mesoscale convective systems and equatorial waves (CCKWs and CCERWs) during extreme rainfall events in Sulawesi, Indonesia. Given the importance of identifying precursors and factors contributing to extreme rainfall events (e.g., Schreck et al. 2020), implementing adjoint-based methods in NWP could offer a promising path toward improving operational forecasts of wave-induced extreme precipitation.

High-resolution convection-permitting (CP) forecasts often operate over a limited area and are nested within global forecast models with parameterized convection and provide potential for improved CCEW forecasting (Jones et al. 2023). Using a suite of CP configurations of the Met Office Unified Model (MetUM), Senior et al. (2023) show that the accuracy of forecasts of a CCKW-driven extreme rainfall event in Padang, Sumatra, on 21 August 2017, depends significantly on the fidelity of the representation of the CCKW in the global model, when the CCKW lies outside of the convection-permitting domain.

The CCKW initiated in the Indian Ocean at around 80°E on 19 August 2017 and propagated to West Sumatra on

21 August, interacting with and intensifying the local diurnal cycle via the modulating process outlined in section 2c. This led to reports of flooding in the Indonesian city of Padang (Fig. 10a). The westerly phase of the CCKW is clearly visible over the CCKW trajectory (shown by red filled contours) and intensifies as it approaches the west coast of Sumatra, resulting in an intensification of the offshore propagating component of the diurnal cycle of rainfall. The parameterized convection global driving model (GAL6) initialized on 0000 UTC 19 August 2017 represented a deterioration in the westerly wind phase of the CCKW, as it propagated over the Indian Ocean (Fig. 10b). By the time the CCKW approached the western boundary of the nested CP model (RAL1T), at 90°E (Fig. 10c), its low-level westerly wind was weak and the CCKW did not appear to propagate into the convection-permitting domain. In the absence of the low-level dynamical CCKW signal, the forecast in the nested model (Fig. 10c) did not show significant rainfall on 21 August 2017. An experiment was conducted where the western boundary of the RAL1T model was extended to 65°E, capturing the region of the initiation of the CCKW and its propagation over the Indian Ocean.

The dynamical component of the CCKW was better represented in the convection-permitting model on the extended domain (Fig. 10d), which simulated more intense low-level westerlies than the global forecast (Fig. 10b). The westerly wind signal weakened near 90°E on 20 August 2021, consistent with observations but reintensified as it approached the west coast of Sumatra. In contrast, in the nested model with a western boundary at 90°E (Fig. 10c), the signal weakened further, as the model inherited a decaying CCKW from the global driving model (Fig. 10b). In Fig. 10d, the westerly anomalies are evident as a weakening of the climatological easterlies east of 90°E, which subsequently turn westerly in the total field by

TABLE 1. Details of the NWP models used in this study. The top two rows are subseasonal models taken from the S2S database (Vitart et al. 2017) where reforecasts are available, providing a longer temporal coverage, at a reduced initialization frequency. The remaining four models are from the TIGGE (Bougeault et al. 2010) archive and are typically shorter range and higher resolution than subseasonal models. For TIGGE models, forecasts from only 2024 at a daily initialization frequency are used, to obtain the most recent version of each model, as reforecasts are not performed for these models.

Model	Initialization frequency	Temporal coverage	Horizontal native resolution (atm) (km)
GloSea6	Four times per month	1993–2016	60
ECMWF (subseasonal)	Two times per week	2003–23	35
ECMWF (medium range)	Twice daily (only 0000 UTC used)	2024	9
ECCC (GEPS)	Twice daily (only 0000 UTC used)	2024	25
DWD (ICON)	Twice daily (only 0000 UTC used)	2024	26.5
NCEP (GEFS)	Four times daily (only 0000 UTC used)	2024	25

100°E. Extending the domain allowed the model to capture the CCKW initiation region and the eastward propagation of these anomalies, resulting in a stronger dynamical signal near Sumatra. Consequently, the extended domain forecast captured more intense precipitation at Padang, linked to an enhanced diurnal cycle within a broad envelope of eastward-propagating convection on 21 August 2021.

These results suggest that extending the boundary of the convection-permitting domains toward the source of tropical forcing leads to significantly improved forecasts, due to reduced boundary errors and a more accurate representation of convective coupling in the parameterized convection domains.

The success of the different approaches described above raises questions about the most effective methods to improve the prediction of wave-related high-impact weather in the MC. While most forecast systems highlight the need to better simulate processes related to the coupling between convection and large-scale circulation in numerical models (e.g., Schreck et al. 2020; Dias et al. 2023; Ferrett et al. 2023; Wolf et al. 2024), reducing CCEW errors (both in amplitude and in propagation speeds) offers another way to significantly improve the operational forecast of wave-induced high-impact weather in the MC in the near future.

b. The representation of equatorial waves and associated precipitation in current numerical models

This section examines how NWP models represent equatorial waves and related precipitation in more detail. It covers Rossby, Kelvin, and MRG waves, as well as the representation of related rainfall. The NWP models used in the figures are detailed in Table 1. Convective-permitting models are also briefly discussed. Figures in this section use the method described in Yang et al. (2021) that allows for dynamical wave filtering of real-time data, enabling wave identification in forecast data. Yang et al. (2021) also introduce a method to calculate the local phase of equatorial waves, using two indices from the identified dynamical wave to fully describe the local phase of the wave at any given time. For example, in the case of the Kelvin wave, equatorial Kelvin 850-hPa zonal wind and equatorial Kelvin wave 850-hPa convergence are used to construct a phase space analogous to the Wheeler–Hendon MJO phase space (Wheeler and Hendon 2004). This allows equatorial wave phase error in forecasts to be quantified.

1) ROSSBY WAVES

Figure 11 shows an example of an observed CCERW event and some reforecast examples from the S2S database (Vitart et al. 2017) to demonstrate the types of wave biases that can be seen in a single case. Reforecasts, also known as hindcasts, are a set of historical forecasts that are run with the current version of the model. The figure shows the event from GPM and ERA5 (Fig. 13a) and reforecasts from control members of the Met Office (UKMO) Global Seasonal Forecasting System, version 6 (GloSea6; MacLachlan et al. 2015) (Figs. 11b,d) and the ECMWF extended range ensemble (Figs. 11c,e). The CCERW occurred in October 2016 and was associated with Typhoon Sarika, which was formed on 13 October 2016 east of the Philippines (Fengjin and Qiufeng 2023). Studies have shown that equatorial Rossby waves can serve as precursors to tropical cyclone formation (Frank and Roundy 2006; Feng et al. 2023; Latos et al. 2023), as seen in this case. Equatorial westerly anomalies associated with a Rossby wave propagate from the Pacific Ocean to the Philippines several days before the formation of the tropical cyclone, as shown by the line contours in Fig. 11a. As discussed in section 2b, these positive zonal wind anomalies over the equator are associated with positive vorticity, convergence, and positive precipitation anomaly in the Northern Hemisphere. There is also a smaller peak in zonal winds that precedes the larger peak by several days, indicating the wave train.

Four reforecasts for this event are shown in Figs. 11b–e. Both GloSea6 and ECMWF reforecasts are initialized on 9 October (Figs. 11b,c). Both capture dynamical Rossby wave activity, though the structure is not as refined as that in ERA5, with longitudinally broader zonal wind anomalies than observed. The two peaks of westerlies propagating one after the other are not shown in reforecasts. The rainfall anomaly associated with the wave is also very weak compared to observations. When the models are initialized later, on 17 October for GloSea6 and 16 October for ECMWF (Figs. 11d,e), the wave activity matches the structure in ERA5 more accurately. However, the wave terminates within the first few days of the GloSea6 forecast and does not propagate past 120°E. The wave persists longer in ECMWF, matching the ERA5 wave more closely. However, the rainfall anomaly associated with the Rossby wave is still underestimated compared to GPM. While errors here are also indicative of the failure of the models to capture Typhoon Sarika, biases in equatorial wave representation
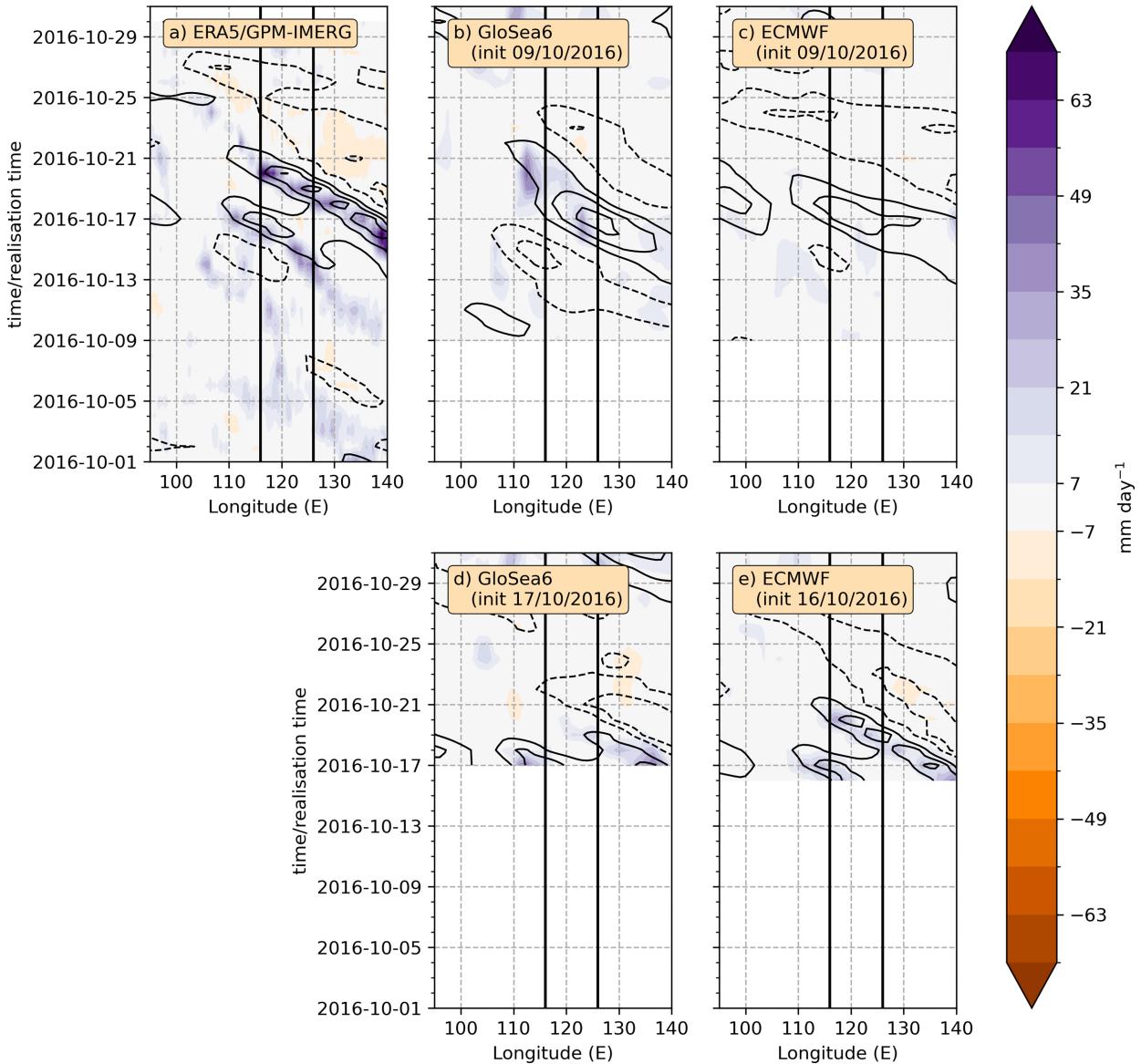
FIG. 11. Hovmöller of daily rainfall anomaly (5°–20°N) during a Rossby wave event in October 2016 for observational/reanalysis datasets and control member of S2S reforecasts. Line contours indicate the 850-hPa Rossby wave zonal wind at the equator using the method of Yang et al. (2021). (a) The event in ERA5 (wave contours) and GPM-IMERG (rainfall) datasets; (b) the event from UKMO GloSea6 reforecast initialized at 0000 UTC 9 Oct 2016; (c) as in (b), but for ECMWF extended-range reforecast initialized on 9 Oct 2016; (d) as in (b), but initialized on 17 Oct 2016; (e) as in (c), but initialized on 16 Oct 2016. Line contours are at intervals of 3 m s^{-1}. NWP rainfall anomalies are relative to their initialization climatology. Philippines longitudinal extents are shown by black vertical lines.

may impact the forecast of typhoons, and vice versa, as the two are inherently linked.

Figure 12 shows the aggregated statistics for $n = 1$ Rossby dynamical wave phase and amplitude in GloSea6 and ECMWF, compared with ERA-Interim and ERA5. These statistics are calculated over all the available S2S reforecasts as detailed in Table 1 and so provide a more generalized view of equatorial wave biases. It is important to note that the reanalysis dataset used for initialization of each ensemble differs. ERA-Interim is used for GloSea6, and ERA5 is used for ECMWF; therefore, statistics for both these

datasets are also shown in the figures. In Figs. 12a and 12b, the amplitude of dynamical Rossby wave activity (represented by the standard deviation of Rossby wave equatorial zonal wind) is shown as a function of longitude and lead time. There is relatively little change in amplitude from the initialization dataset (ERA-Interim) in the days after the reforecast initialization, which is slightly below ERA5 amplitudes (Fig. 12a), though still often within the 95% confidence interval. In ECMWF, the errors in amplitude are larger, and at 8-day lead time, amplitude is reduced by around 15% at all longitudes shown (Fig. 12b).
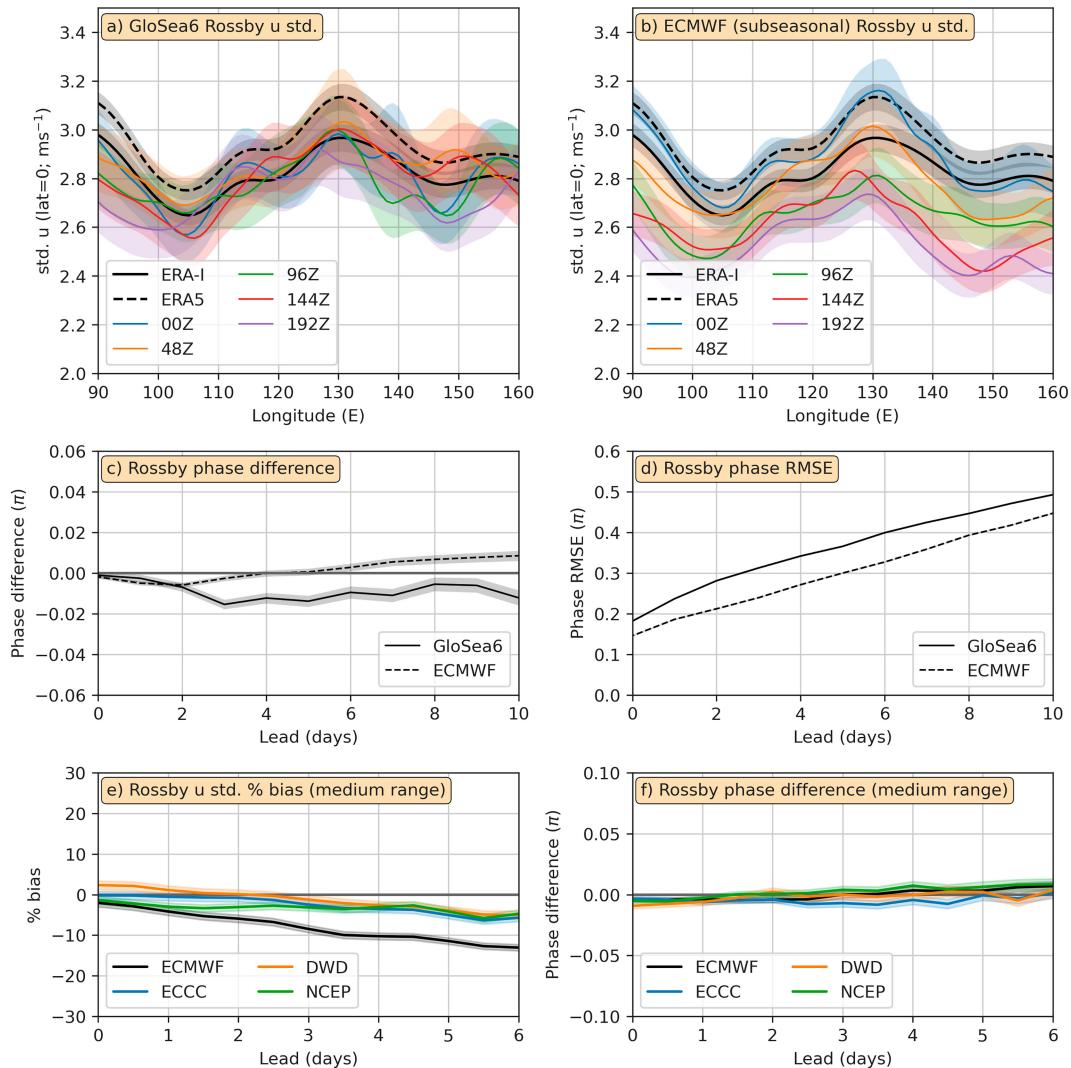
FIG. 12. Aggregated Rossby wave amplitude and phase statistics in UKMO GloSea6 and ECMWF S2S reforecasts and four TIGGE models (control ensemble member). Statistics are calculated using the method of Yang et al. (2021) over all available initializations. (a) GloSea6 standard deviation of R1 wave 850-hPa equatorial zonal wind as a function of longitude; (b) as in (a), but for ECMWF; (c) phase difference as a function of lead time for GloSea6 (solid) and ECMWF (dashed) relative to their initialization datasets; (d) phase RMSE as a function of lead time relative to their initialization datasets; (e) medium-range TIGGE model equatorial zonal wind bias averaged over 90°–160°E (% relative to the relevant analysis) as a function of lead time; (f) TIGGE model average Rossby wave phase difference over 90°–160°E as function of lead time. In (a) and (b), colored lines indicate varying lead time and black lines show ERA-Interim (solid) and ERA5 (dashed). In (e) and (f), colored lines indicate different TIGGE models (see Table 1 for more details). Shading shows the 95% confidence interval calculated using bootstrapping with 10 000 resamples.

Phase is calculated as described at the start of this section following the methodology of Yang et al. (2021), where a local phase space is constructed using dynamical fields of wave activity. Differences in phase between the model and observations are between $-\pi$ and π in the phase space, where a difference of $-\pi$ or π (-1 or 1 on the y axis) indicates that an opposite phase to that observed is forecast in the region of interest (e.g., divergence instead of convergence, eastward wind instead of westward wind). The sign shows the direction of bias, where a negative difference implies the forecast wave is

shifted toward the west, which can be indicative of faster propagation speed for Rossby waves. A positive difference is indicative of a slower propagation speed. Phase errors in both models are relatively small for the Rossby wave, suggesting that there is no consistent bias in either direction. Since the difference metric is averaged over many waves and initialization times, the value is only representative of a systematic bias in one direction or another. This is why the difference may decrease at longer lead times, since the errors in wave location become larger and are less related to a propagation

bias, but rather a more general bias in wave location and initiation, which could be unrelated to observed wave location. Figure 12d shows the root-mean-square error (RMSE) of phase (the 95% confidence interval is comparatively small, ≈ 0.002), which is more indicative of the spatial error in wave patterns without implied direction. This increases steadily with lead time and reaches 0.4π at lead day 6 in GloSea and at lead day 8 in ECMWF. A value of $\pi/2$ indicates, on average, an entirely different phase than that in observations.

Figure 12 also shows amplitude and phase biases for four medium-range NWP models taken from the THORPEX Interactive Grand Global Ensemble (TIGGE; Bougeault et al. 2010) archive, to demonstrate the range of equatorial wave biases from different NWP models. Amplitude bias is shown using average (90°–160°E, all initialization times) bias as a percentage relative to the appropriate analysis as a function of lead time (Fig. 12e). Phase bias is shown using average (90°–160°E, all initialization times) phase difference as a function of lead time (Fig. 12f). The four models used are the medium-range ECMWF model, Icosahedral Nonhydrostatic (ICON)-Ensemble Prediction System (EPS) from DWD (Zängl et al. 2015), Global EPS (GEPS) from Environment and Climate Change Canada (ECCC) (Lin et al. 2016), and GEFS from National Centers for Environmental Prediction (NCEP) (Zhou et al. 2022). For the Rossby wave, amplitudes are consistently underestimated (Fig. 12e), with amplitudes around 5%–10% weaker in all models at lead day 5. However, there are relatively small average phase differences in all four TIGGE models at all lead times up to day 6 (Fig. 12f), consistent with the subseasonal models (Fig. 12c).

Yang et al. (2021) examine dynamical Rossby wave variability in a UKMO NWP model and find similar results, suggesting that amplitude errors in Rossby waves relative to initialization are relatively small. However, it is possible that biases may differ by season and therefore appear small as an annual average; Yang et al. (2023) found, in an earlier version of the GloSea model, that Rossby wave activity over the MC is overestimated in winter and spring months and underestimated in summer and autumn months.

2) KELVIN WAVES

Figure 13 shows an example of an observed and reforecast CCKW event. The depicted CCKW event occurred in June 2016 and impacted Peninsular Malaysia and parts of Indonesia. The wave signal is shown in ERA5 to the west of Peninsular Malaysia (longitudinal extents of Peninsular Malaysia shown by black vertical lines) around 15 June. The wave convergence (dashed line contours in Fig. 13a) coincides with a large positive daily rainfall anomaly (colored shadings in Fig. 13a). The wave propagates eastward in subsequent days passing over Peninsular Malaysia and Borneo, resulting in heavy rainfall in both regions.

GloSea6 reforecasts for two separate initialization dates are shown in Figs. 13b and 13d. The first is around a week before the CCKW is visible in GPM and ERA5, at 0000 UTC 9 June (Fig. 13b). The dynamical wave signal is visible in the reforecast from 17 June to the east of Peninsular Malaysia, a

day or two later than ERA5 and weaker in amplitude. The propagation speed of the wave is also faster than the observed wave, with the convergence associated with the wave reaching 130°E by around 18 June in GloSea6, compared to around 21 June in ERA5. The rainfall anomaly associated with the CCKW is also substantially weaker than that of GPM-IMERG. For the later initialization time (Fig. 13d), the amplitude of the convergence associated with the wave is similarly weak, indicating that biases in Kelvin wave amplitude can develop within the first few days following forecast initiation. Propagation speed errors are still present at the later initialization time, though there are improvements compared to the earlier initialization time; Kelvin wave convergence reaches 130°E around 20 June, 1 day earlier than ERA5.

Recent iterations of the ECMWF system have been found to represent equatorial waves better than previous NWP systems (e.g., Janiga et al. 2018; Dias et al. 2023). However, in this case, ECMWF reforecasts have similar issues to GloSea6, as shown in Figs. 13c and 13e. The ECMWF reforecast initialized at 0000 UTC 10 June is used for the earlier initialization time. This performs slightly worse than GloSea6, with larger errors in the CCKW convergence amplitude and a further reduced rainfall signal (Fig. 13c). For the later initialization time, on 17 June, as in GloSea6, the amplitude of the wave convergence is improved. However, the rainfall anomaly is still too weak, and the CCKW also propagates too quickly compared to ERA5 (Fig. 13e).

Previous studies highlight these types of errors in Kelvin waves across numerous NWP systems at a range of temporal scales. In fact, Yang et al. (2021) analyze wave statistics in the UKMO global operational deterministic forecast model and find that the Kelvin wave shows stronger biases than westward-propagating waves. Kelvin waves in forecasts are typically too weak and tend to occur further east compared to observations, which may result from faster propagation speeds or spatial initiation biases. Yang et al. (2021) find that the magnitude of biases varies with longitude, and the largest phase errors occur over the MC. Ferrett et al. (2023) find that the UKMO Global and Regional EPS (MOGREPS) skill to forecast the phase of Kelvin waves drops quickly, and NWP forecasts are often less skillful than a climatological forecast of wave phase after a 1–2-day lead time. Dias et al. (2023) examine the power spectra of precipitation in recent ECMWF reforecasts and find an underestimation of the amplitude of convective activity associated with CCKWs, as well as errors in phase. Similarly, Janiga et al. (2018) find underestimation of CCKW variability in a number of subseasonal forecast systems. However, they also find that one of the three systems they examined overestimates Kelvin variability in the MC, highlighting bias inconsistency in different systems.

Figure 14 shows aggregated biases in amplitude and phase of the dynamical component of the Kelvin wave for the GloSea6 and ECMWF extended-range reforecasts. Amplitude is represented by the standard deviation of the Kelvin wave–associated 850-hPa zonal wind at the equator and is shown as a function of longitude and lead time in Figs. 14a and 14b for both subseasonal NWP ensembles. For GloSea6, the amplitude of wave activity is weaker than ERA5 and increases with
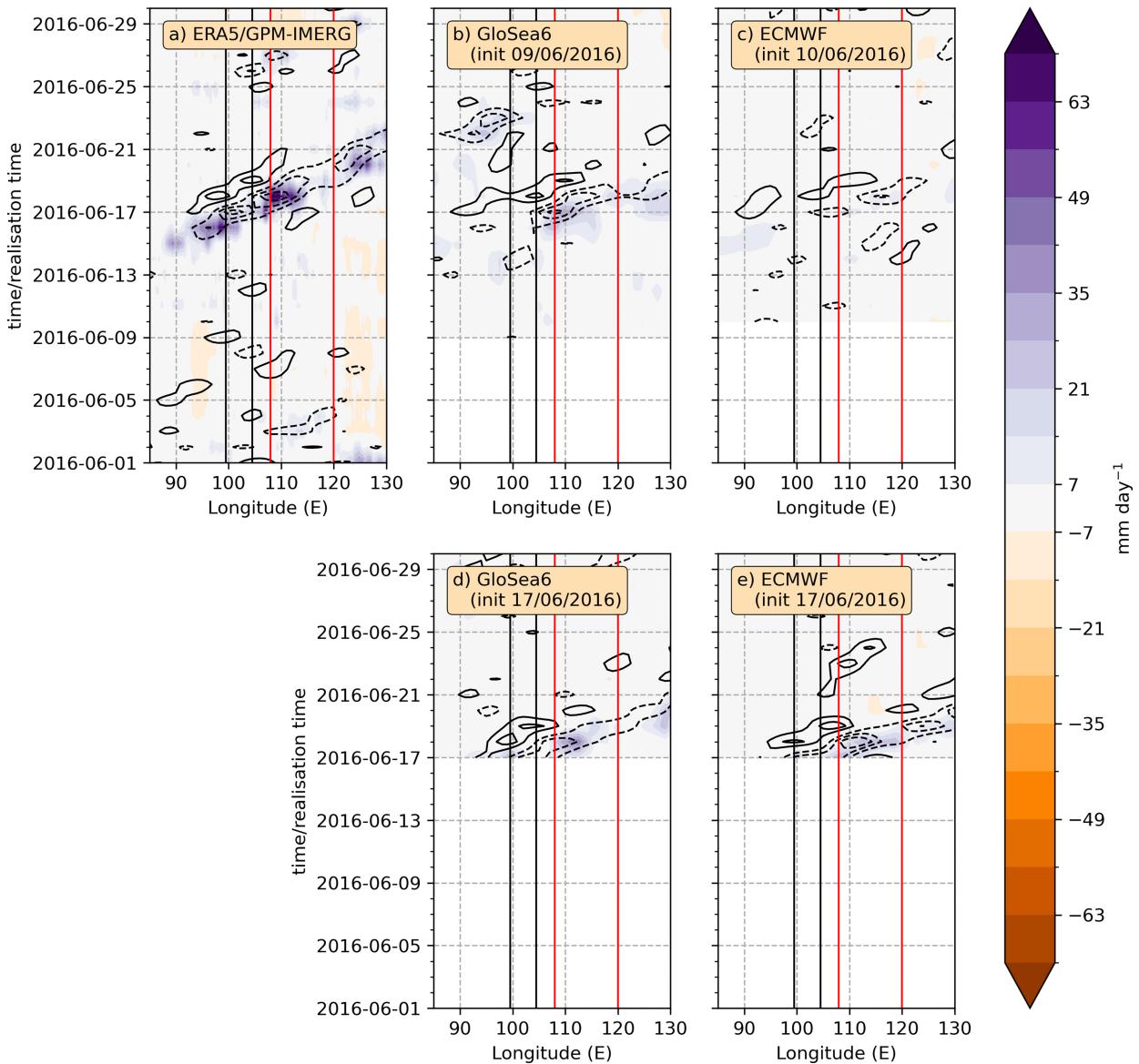
FIG. 13. As in Fig. 11, but for a Kelvin wave event in June 2016. Rainfall is averaged between 5°S and 5°N. Line contours indicate the 850-hPa Kelvin wave divergence at the equator using the filtering method of Yang et al. (2021), at an interval of 2^{-6} s^{-1}. Peninsular Malaysia and Borneo longitudinal extents shown by black and red vertical lines, respectively.

lead time to more closely match ERA5 values, though refore-casts underestimate wave activity relative to ERA5 at earlier lead times. For ECMWF, CCKW amplitude drops quickly with lead time and is underestimated, relative to ERA5, at longer lead times (>4 days lead time). Both models underesti-mate the amplitude of wave activity relative to ERA5 (the more recent reanalysis) at times, in agreement with previous studies that suggest underestimation of CCKW activity is common in NWP models (Yang et al. 2021; Dias et al. 2023; Yang et al. 2023; Cruz et al. 2024; Gehne et al. 2022). This depends on lead time in each model, and amplitude is underestimated relative to ERA5 at earlier lead times in GloSea6 (<4 days lead) and at later lead times in ECMWF

(>4 days lead). As shown here, initialization data have an effect on amplitude bias.

CCKW phase errors in the two models, relative to their initial-ization dataset, over 90°–160°E, are shown in Figs. 14c and 14d. In this case, both models have a positive phase difference, sug-gesting faster propagation speeds (as the Kelvin wave propagates eastward). This difference is larger in ECMWF than in GloSea6, particularly at shorter lead times. The phase RMSE increases steadily with lead time 13. At around lead day 7 in GloSea6 and lead day 10 in ECMWF, the RMSE reaches $\pi/2$. These results demonstrate persisting phase errors in current NWP systems and are consistent with previous studies that find that propagation speeds of CCKWs are too fast in UKMO,
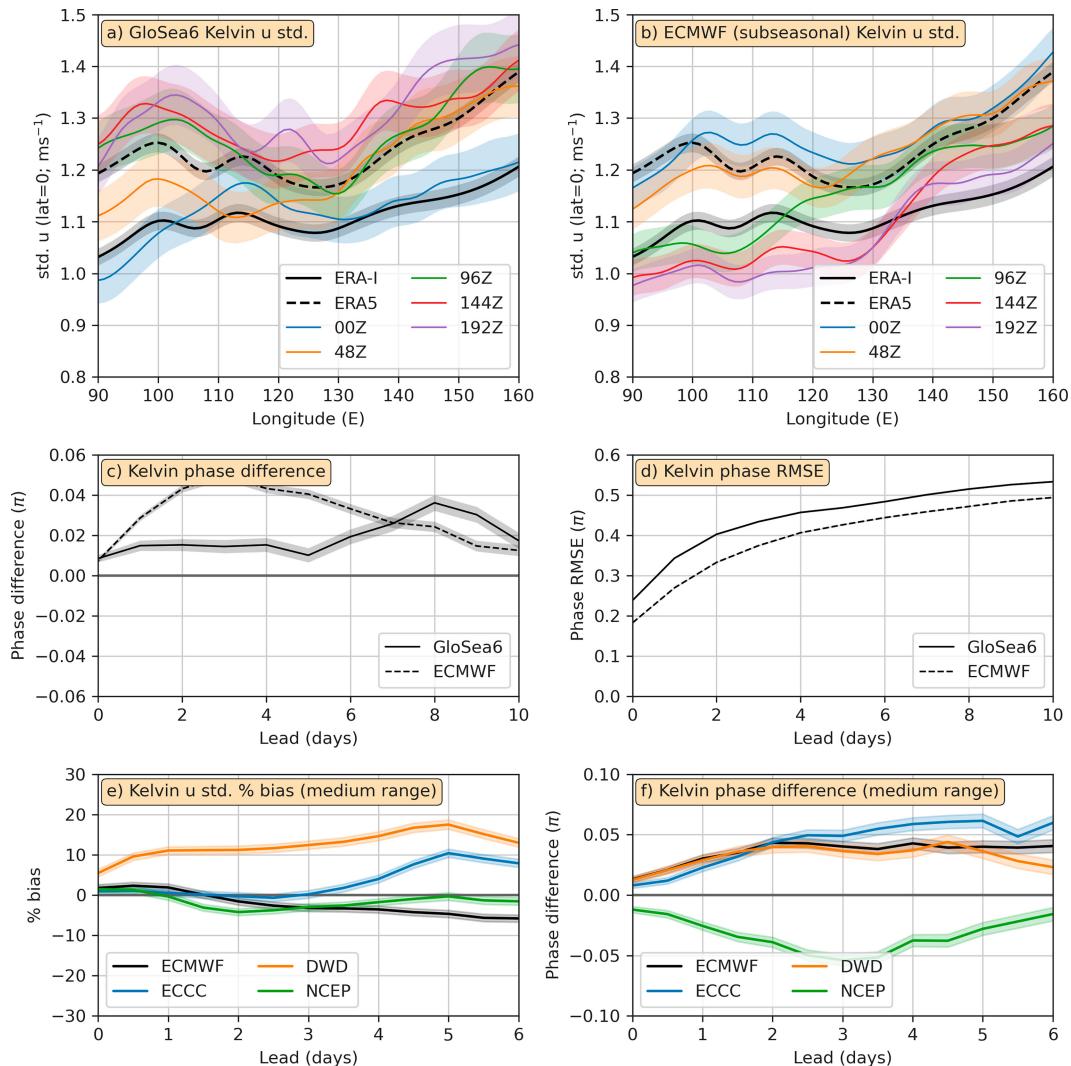
FIG. 14. As in Fig. 14, but for Kelvin waves.

ECMWF, and other NWP models (Dias et al. 2018, 2023; Yang et al. 2021, 2023; Gehne et al. 2022; Bengtsson et al. 2019).

In medium-range models, Kelvin amplitude biases vary depending on the model. The DWD model shows the largest bias, with amplitudes almost 20% too strong relative to analysis at lead day 5 (Fig. 14e). The ECCC model also overestimates Kelvin wave amplitude at lead times greater than 4 days, with an overestimation of 10% at lead day 5. NCEP and ECMWF models have smaller biases and slightly underestimate amplitudes as lead time increases (up to around 5% underestimation). There are also some differences between models for phase biases, with NCEP having a negative phase difference at all lead times, while the remaining three models have a positive phase difference throughout, consistent with the subseasonal models (Fig. 14f). This demonstrates that Kelvin wave biases can be dependent on the model used.

3) MRG WAVES

An example of an MRG wave, which was associated with heavy rainfall and flooding in Thailand, is shown in Fig. 15. During the event, an MRG wave packet propagates from over the Indian Ocean toward Thailand. On 1 December 2016, strong MRG Southern Hemisphere easterlies (associated with the positive vorticity phase of the wave) occurred around 100°–110°E. The wave then propagates westward, coinciding with increased daily rainfall over Thailand and Peninsular Malaysia in the subsequent days. A GloSea6 reforecast initialized on 25 November, which is 6 days prior to the event, does not capture the event at all showing very little evidence of wave activity and increased rainfall (Fig. 15b). ECMWF performs better with a reforecast initialized on the 27 November by capturing the wave activity well, though the associated rainfall is underestimated (Fig. 15c). Reforecasts with a later initialization time (1 December for GloSea6; 4 December for ECMWF) capture both the wave activity
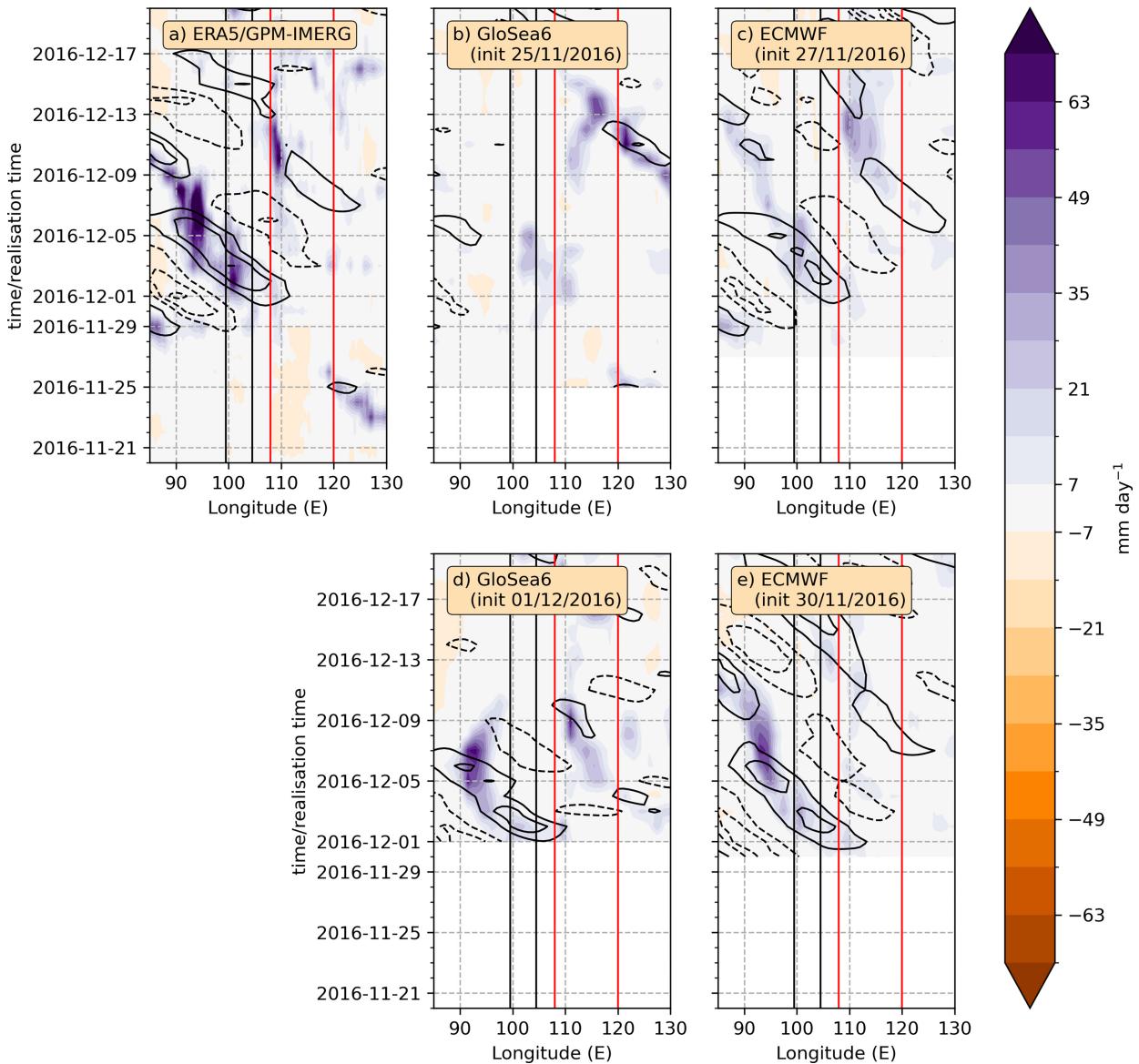
FIG. 15. As in Fig. 13, but for an MRG wave event in December 2016. Rainfall is averaged between 5° and 15°N. Line contours indicate the 850-hPa MRG wave zonal wind at 8°S using the filtering method of Yang et al. (2021), at an interval of 1.33 m s^{-1}.

and the associated rainfall better (Figs. 15d and 15e). ECMWF is able to capture the MRG wave activity at longer lead times, in contrast to GloSea6, which only captures wave activity when initialized during the event. As with the Kelvin and Rossby wave cases discussed above, accurate forecasting of heavy rainfall events associated with MRG waves is limited to short lead times in both models.

Amplitude and phase errors of MRG in the models are shown in Fig. 16. Results are similar to the Rossby wave, such that GloSea6 amplitudes are close to the initialization dataset, ERA-Interim, even at longer lead times (up to 8 days). However, ECMWF MRG amplitude decreases from the initialization time, and by 8-day lead time, amplitudes are weaker than both reanalyses. Both models exhibit negative phase errors,

which are larger in GloSea6 than in ECMWF (Fig. 16c). This is indicative of persistent biases, which can relate to faster propagation speeds. In ECMWF, errors are positive at longer lead times (greater than 6 days), indicating slower propagation speeds, and then tend toward zero. Phase RMSEs increase with lead time at a faster rate than Rossby wave errors in both models but at a slower rate than Kelvin wave errors (Fig. 16d).

MRG amplitude is generally underestimated in medium-range TIGGE models (Fig. 16e), consistent with the subseasonal models. ECMWF shows the largest bias, with an underestimation of the amplitude of around 20% at lead day 5. The remaining three models have less severe biases; all have less than 10% underestimation at lead day 5. DWD and ECCC models have the least
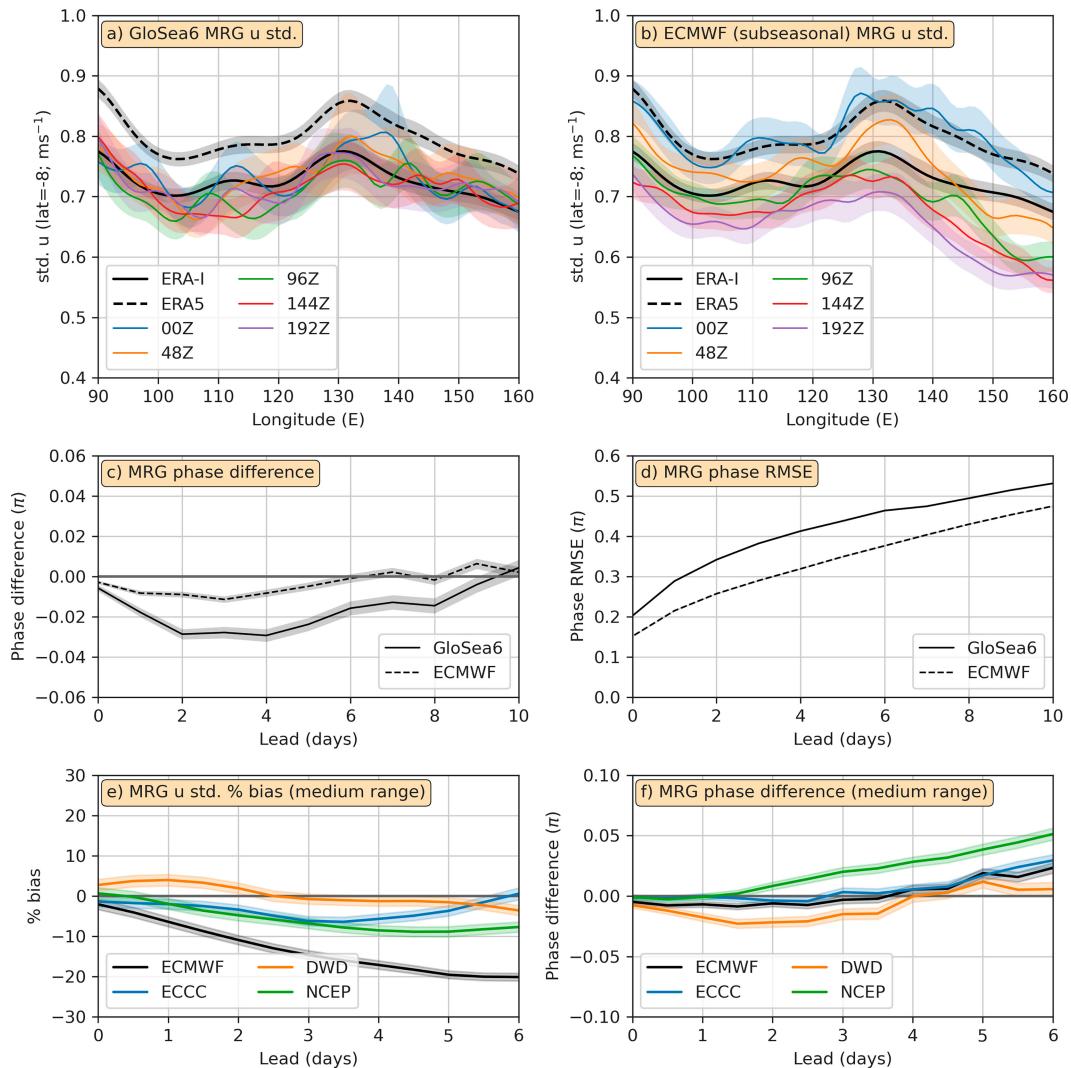
FIG. 16. As in Fig. 14, but for MRG waves. For (a), (b), and (e), 850-hPa zonal wind is taken at 8°S.

bias in Kelvin wave amplitude at longer lead times (>4 days). All four TIGGE models have a positive phase bias (propagating too slow) at lead times longer than 4 days, with the largest phase bias in NCEP and the smallest bias in DWD (Fig. 16f). While there is a range of values in the extent of MRG amplitude and phase biases, the sign tends to be consistent between the four models. There is an underestimation in amplitude and, as in subseasonal models, a negative phase bias (propagating too fast) at early lead times (up to 2–4 days for TIGGE models) and a positive phase bias at longer lead times (greater than 4 days).

The statistics shown here are consistent with previous analyses that focus on forecasts of MRG waves, which tend to find that MRG variability is slightly underestimated in NWP models relative to observations (Dias et al. 2023; Yang et al. 2021, 2023). There are relatively few studies that quantify MRG phase errors in NWP models, though Yang et al. (2021) show MRG waves propagate slower than observed in a UKMO operational global forecast. The results here suggest that the sign

of the MRG phase bias may vary depending on the model and lead time.

While forecast biases are present for all three wave types, in general, westward-propagating waves tend to be better represented in NWP models than Kelvin waves (Yang et al. 2009, 2021, 2023; Goswami et al. 2017; Janiga et al. 2018). There has yet to be an in-depth study comparing the underlying sources of biases in different wave types, and so this is an open research question. However, there are a number of possible reasons. Kelvin waves are more strongly coupled to deep convection and moist processes (Wheeler and Kiladis 1999; Kiladis et al. 2009), making them highly sensitive to convective parameterizations, model resolution, and mean-state errors (Maher et al. 2018; Judt and Rios-Berrios 2021; Yang et al. 2021). In contrast, Rossby wave $n = 1$ (R1) and westward-propagating MRG (WMRG) waves are more weakly coupled to convection and therefore more directly constrained by dry dynamical balances, which may reduce their sensitivity to these model deficiencies.

4) CCEW-RELATED RAINFALL

Previous studies suggest that CCEW biases could be related to the representation of convection in NWP models (Yang et al. 2021, 2023). NWP models can struggle to capture convection accurately, and this may have a direct link with the representation of CCEWs. In this section, the representation of rainfall during CCEW events is examined. Here, the focus is on the representation of rainfall in general, as opposed to extreme rainfall in particular, since this is where the majority of current literature is focused. Ferrett et al. (2020) show that an increase in mean rainfall during equatorial waves is also associated with an increase in the likelihood of extreme rainfall; therefore, the representation of average rainfall during equatorial waves is a good starting point to assess how rainfall extremes may be represented. However, the representation of extreme rainfall associated with equatorial waves should certainly be an area of future study.

Figure 17 shows composites of observed equatorial wave events in varying regions of the MC and the biases in subseasonal reforecasts of those same days. Figures 17a–c show composites of days when Rossby wave–related 850-hPa vorticity is over the Philippines for reanalyses/observations (Fig. 17a) and the GloSea6 (Fig. 17b) and ECMWF (Fig. 17c) reforecast biases of the same days at 3–5-day lead time (where the required initialization time is available). The figure in appendix C shows the GPM-IMERG/ERA5 composite for the same days used in the reforecast bias composites (Fig. C1). In GPM-IMERG, there is a large positive rainfall anomaly associated with the positive vorticity of the Rossby wave, partly a result of related tropical cyclones (Fig. 17a). In both GloSea6 and ECMWF reforecasts, the rainfall anomaly is substantially weaker over the ocean. Using the false discovery rate method (Wilks 2016), most decreases over land in Figs. 17b and 17c are not statistically significant (not shown). While there are some biases in the ocean rainfall anomaly, the models are able to capture the location of the dynamical structure of the Rossby wave well (Figs. 17b,c).

Figures 17d–f show composites of days when Kelvin wave 850-hPa convergence is over Borneo. In observations/reanalysis, there is a strong positive rainfall anomaly coinciding with the location of Kelvin wave convergence (Fig. 17d), as described in previous sections. In the reforecasts, the rainfall anomaly is smaller than in GPM-IMERG. GloSea6 performs reasonably well over land, although positive rainfall anomalies tend to be too weak, especially north of Borneo, over the Java Sea and Makassar Strait (Fig. 17e). ECMWF shows a positive rainfall anomaly that is too weak over Borneo. The positive rainfall anomaly is too strong to the east of Borneo, over the ocean in both models (Figs. 17e,f). This is likely due to the location of the center of Kelvin wave convergence, which is shifted to the east, consistent with faster propagating waves in the models compared to observations (Fig. 14c). These biases show that Kelvin wave–related heavy rainfall days are underestimated in the reforecasts, particularly in ECMWF, as early as 3-day lead time.

Rainfall in southern Thailand and Peninsular Malaysia associated with the MRG wave is examined in Figs. 17g–i. In observations, a positive rainfall anomaly is collocated with horizontal wind convergence in the Northern Hemisphere, on the northwest edge of the MRG-related cyclonic gyre (Fig. 17g). These patterns are well replicated in the models, especially in ECMWF (Fig. 17i). In contrast, in GloSea6, the gyre is weaker, leading to an underestimated rainfall anomaly over southern Thailand (Fig. 17h).

It is clear from these figures that substantial biases in equatorial wave–related rainfall exist at early lead times in NWP forecasts, and rainfall extremes associated with equatorial waves are likely to be underestimated. Previous studies showed that convective activity associated with equatorial waves tends to be underestimated in subseasonal NWP models, relative to observations (Dias et al. 2023). Furthermore, NWP models show much less predictability in rainfall associated with equatorial waves than theory would suggest. For example, Li and Stechmann (2020) investigate the predictability of tropical rainfall associated with CCEWs using observations and find that the predictability from CCERWs is 8–12 days and from CCKWs is 2–3 days. In contrast, studies using S2S forecasts show that the majority of rainfall variability is dominated by low-frequency variability and MJO-related variability, with CCEWs contributing relatively little (Janiga et al. 2018; Schreck et al. 2020). Our study clearly indicates that model fidelity in representing CCEW activity is closely linked to uncertainties in extreme precipitation forecasts and limits the predictability of hazardous weather over the MC region.

Convection-permitting models provide a step forward in forecasting equatorial wave–related rainfall. Judt (2020) finds that CCEW-related rainfall is substantially better represented in a higher-resolution model that resolves convection explicitly (e.g., a 4-km horizontal resolution) than a model with coarser resolution and parameterized convection (e.g., >10-km horizontal resolution). Judt and Rios-Berrios (2021) also show that Kelvin wave activity and related rainfall are more accurately captured in convection-resolving models and suggest that resolving convection plays a larger role in improving wave-related rainfall than increasing resolution. Ying and Zhang (2017) also find that there is predictability in Rossby, Kelvin, and MRG waves for at least 8 days in a convection-permitting limited-area ensemble. However, they point out that wave-associated precipitation has limited predictability compared to other variables, such as winds, temperature, and humidity.

Past studies show that convection schemes and their parameters play an important role in the modeling of the MJO (Zhou et al. 2012; Liu et al. 2019). Differences in convection schemes may also play a role in equatorial waves and related rainfall. Bengtsson et al. (2019) use the ECMWF Integrated Forecasting System (IFS) convection scheme in a version of the National Oceanic and Atmospheric Administration's (NOAA) Global Forecast System (GFS) to investigate the role of the convection scheme in equatorial wave simulation. They find that there are improvements in modeled equatorial waves, such as more coherent convection propagation, using the IFS scheme compared with the GFS default configuration as a result of improved convection and circulation interactions. Goswami et al. (2017) introduce a stochastic convective parameterization to the NCEP Climate Forecast System (CFS), version 2, and find significant improvements in
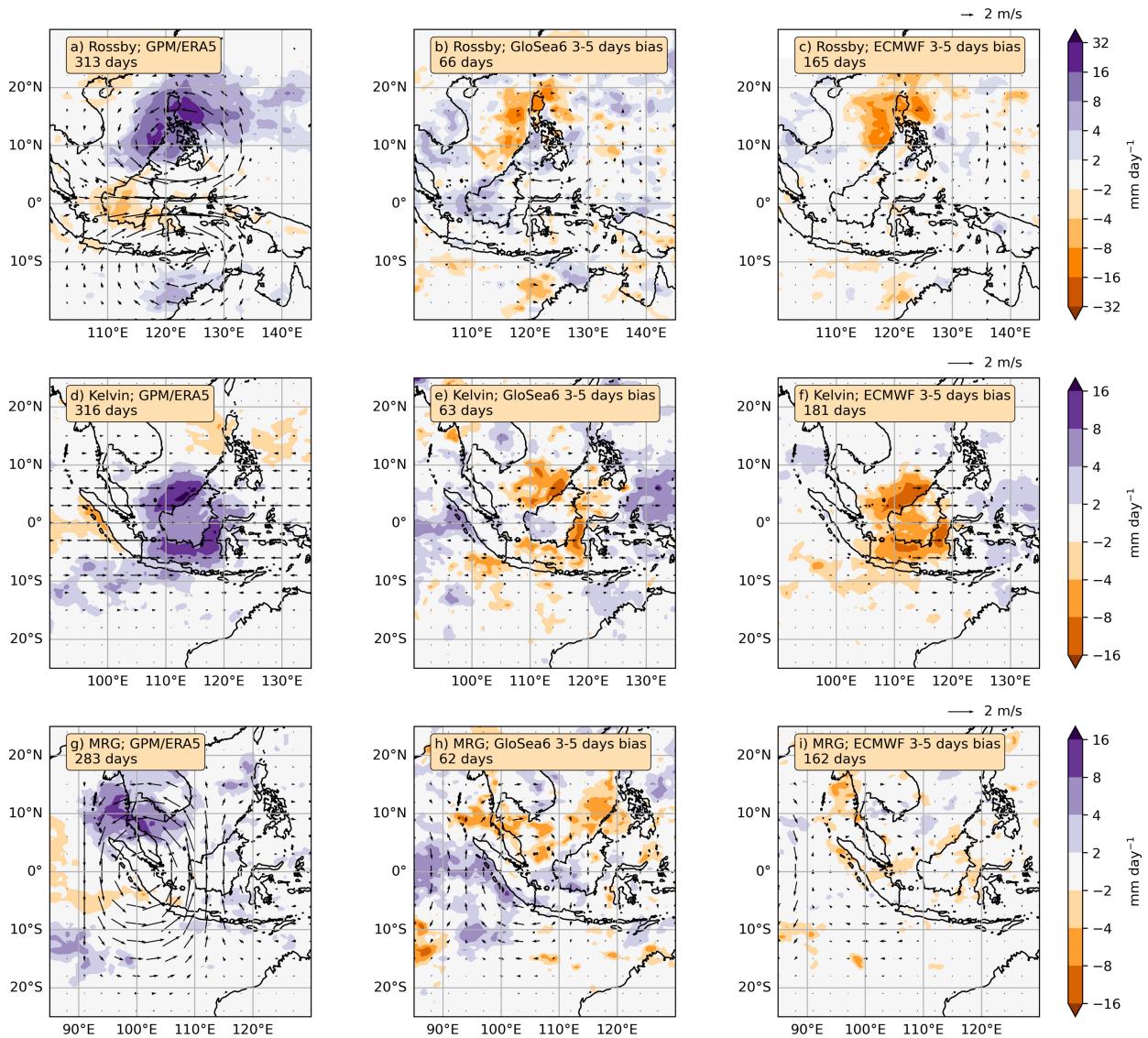
FIG. 17. (a),(d),(g) Daily rainfall anomaly composites for GPM-IMERG and (b),(e),(h) the difference between the control ensemble member of GloSea6 lead days 3–5 and GPM-IMERG, and (c),(f),(i) the difference between the control member of subseasonal ECMWF lead days 3–5 and GPM-IMERG. (a)–(c) Composites are on days with ERA5 Rossby wave 850-hPa positive vorticity over Philippines (positive vorticity over 120°–125°E), (d)–(f) Kelvin wave 850-hPa convergence over Borneo (convergence over 110°–115°E), and (g)–(i) MRG 850-hPa positive vorticity over Sumatra (positive vorticity over 100°–105°E). Vectors show the wave-filtered horizontal wind field at 850 hPa using the Yang et al. (2021) method. Composites were calculated from year-round ERA5 and GPM data (2001–22) and reforecast data from 2000 to 2016 for GloSea6 and 2004–22 for ECMWF. For the differences in (b), (c), (e), (f), (h), and (i), differences are relative to GPM-IMERG/ERA5 on the corresponding dates available for the model (Fig. C1 in appendix C). The total number of events in each composite is shown in the panel title.

the simulation of the MJO and CCEWs. Section 3a provides a comprehensive discussion of biases in convection schemes and their implications for tropical wave activity.

4. Recommendations for future research and forecasting

a. Possibilities for future improvements in models

As discussed in section 3, the variance of CCEWs in most global operational NWP systems is systematically underestimated

compared with reanalyses and observations. This bias is consistent across deterministic forecasts and ensembles: Wave amplitudes are too weak, Kelvin waves often propagate too quickly, and equatorial Rossby activity is reduced (Dias et al. 2023; Yang et al. 2021; Gehne et al. 2022; Yang et al. 2023; Dias et al. 2018; Janiga et al. 2018). At the grid spacings of global NWP models (~9–13 km for deterministic forecasts), deep convection cannot be explicitly resolved—individual plumes are on the order of 1–3 km. Therefore, convection must

be parameterized, meaning its average effect on the large-scale column is represented statistically (Bauer et al. 2015). The aim of these schemes is to represent the role of convection in removing instabilities generated by radiation, surface fluxes, or large-scale convergence, while providing heating, moistening, and precipitation tendencies (Plant and Yano 2015; see Fig. 2 of Bauer et al. 2015 for key processes parameterized in current NWP models). In doing so, they parameterize key processes central to tropical wave dynamics: entrainment and detrainment, downdrafts and cold pools, latent heating profiles, and sometimes convective momentum transport (Arakawa 2004; Bechtold et al. 2008).

The choice of convection scheme, as well as how its parameters are tuned, strongly influences how tropical wave activity is represented (Liu et al. 2019). Several limitations in convection parameterization common in global NWP systems (such as those listed in Table 1) include the following:

- Instability removed too quickly
  Some schemes consume CAPE on unrealistically short time scales (Bengtsson et al. 2019), suppressing the moist buildup seen before active wave phases and reducing wave–convection coupling (Straub and Kiladis 2003; Mapes 2000; Holloway and Neelin 2009).
- Vertical heating too top heavy
  NWP models have been shown to place convective heating too high in the troposphere, unlike observations that show midlevel heating with low-level cooling from stratiform precipitation. This bias weakens wave forcing and contributes to errors in Kelvin wave speed, Rossby wave amplitude, and MJO propagation (Jiang et al. 2009; Bengtsson et al. 2019). However, modifications in the ECMWF IFS scheme have improved this top-heavy bias (Bechtold et al. 2008; Bengtsson et al. 2019; Bechtold et al. 2014).
- Wrong humidity regime
  Observations show that deep convection is strongly suppressed in dry midtropospheric conditions and increases sharply as the environment moistens (Sherwood 1999; Bretherton et al. 2004; Holloway and Neelin 2009; Derbyshire et al. 2004). Parameterized convection often fails to capture this behavior, triggering too easily in dry columns and producing spurious drizzle while underestimating intense convection in moist conditions. Experiments and model developments demonstrate that increasing entrainment strengthens the dependence of convection on environmental humidity, which reduces drizzle biases and improves the simulation of tropical variability (Bechtold et al. 2008, 2014; Klingaman and Woolnough 2014; Hannah and Maloney 2011).
- Missing mesoscale organization
  Observations show that squall lines, cold pools, and mesoscale convective system clustering shape vertical heating structures and are central to tropical wave dynamics (Lin et al. 2004; Mapes et al. 2006; Crook et al. 2024). Current global NWP models cannot explicitly resolve this organization at ~10-km grid spacing, leading to overly smooth diabatic heating fields and weaker wave coherence (Hannah and Maloney 2011; Grabowski 2003; Bechtold et al. 2008).

- Simplified convective momentum transport
  Observations show that convection redistributes momentum vertically through updrafts, downdrafts, and mesoscale circulations, influencing the propagation of equatorial waves (Tung and Yanai 2002). Many NWP systems omit or oversimplify this process. Studies demonstrate that including convective momentum transport improves tropical variability (Richter and Rasch 2008; Zhang and Wu 2003).

When models operate at convection-permitting resolutions (≤8 km), the representation of tropical waves, their amplitude, structure, and convective coupling significantly improves (Clark et al. 2016; Holloway et al. 2012; Judt and Rios-Berrios 2021; Weber et al. 2020). Likewise, superparameterization experiments (embedding cloud-resolving models within each GCM column) demonstrate more realistic equatorial variability (Randall et al. 2003). The challenge is cost: Convection-permitting forecasts are computationally expensive, and superparameterizations are slower than standard convection schemes, limiting their operational use.

Nested convection-permitting models are often used as a compromise, embedding high-resolution domains within global models (Holloway et al. 2012; Warner 2010). They not only offer clear advantages for representing local convection and wave structures but also face important challenges. A spinup period is usually required before realistic convection develops, during which equatorial waves may be poorly represented (Short and Petch 2022; Warner et al. 2023). Boundary zones also generate artifacts that can distort wave signals, limiting reliability to the inner domain (Ahrens and Leps 2021). Moreover, most nested systems lack full data assimilation and rely on global model initial conditions and boundary forcing, constraining their ability to independently initiate or sustain waves. Recent work shows that forecast skill improves when domains are extended to include upstream regions of wave initiation (Senior et al. 2023; Jones et al. 2023, as discussed in section 3a), underscoring both their potential and their dependence on parent model forcing. Recent global storm-resolving simulations not only show much stronger equatorial wave variability but also highlight the continuing uncertainties in representing shallow convection and upscale convective organization (Satoh et al. 2019; Stevens et al. 2019). Even at convection-permitting scales, shallow convection and aspects of mesoscale organization are still parameterized, which can influence tropical wave variability (Clark et al. 2016).

Between about 3- and 10-km grid spacing, models enter the convective gray zone, where convection is partly resolved but still partly subgrid. Here, conventional parameterizations either double count resolved convection or suppress it (Field et al. 2023; Honnert et al. 2020). To address this, scale-aware or blended schemes have been developed that taper tendencies as resolution increases (Field et al. 2023; Arakawa et al. 2011; Tomassini et al. 2023). These approaches are increasingly important as NWP centers push toward ~5-km global forecasts.

Even with improved convection physics, mean-state errors remain a fundamental source of bias in representing equatorial modes such as the MJO. Dias et al. (2023) find that the amplitude of mean precipitation biases in ECMWF IFS forecasts

(which generally show better representation of tropical waves than other NWP models) is similar to the amplitude of anomalies associated with equatorial waves. Numerous studies suggest that errors in MJO activity subseasonal reforecasts are related to mean-state biases (e.g., Kim et al. 2019; Kim 2017). These biases include long-standing SST errors, ITCZ misplacement and double ITCZ biases, and vertical shear errors, all of which distort equatorial waveguides and their preconditioning environments, suppressing tropical variability even in higher-resolution models (Judt and Rios-Berrios 2021; Kim 2017). Despite these mean-state biases being widely known, there is currently no systematic study quantifying their feedback onto tropical wave activity across NWP systems.

Some recommendations for reducing equatorial wave biases in NWP models include the following:

1) Improving convection parameterization by making schemes more moisture sensitive, adjusting vertical heating structures, and incorporating updrafts, downdrafts, and cold-pool effects. Addressing missing processes by including or improving representations of convective momentum transport and mesoscale organization such as squall lines and mesoscale convective systems.

2) Pushing toward convection-permitting resolutions on global or pan-tropical domains where computationally feasible, while advancing scale-aware approaches in the gray zone (3–10-km resolution). Also, leveraging nested convection-permitting models cautiously: using them to improve local convection and wave representation, extending domains to cover upstream initiation regions, and developing techniques to reduce boundary artifacts and accelerate spinup.

3) In convection-permitting regimes, continuing to improve shallow convection and cloud microphysics parameterizations, since these remain critical for the realistic representation of tropical variability.

4) Tackling background state errors by reducing biases in humidity, stratification, vertical shear, and cloud-radiative interactions. This can be achieved by improving data assimilation and observational coverage to initialize models, especially moisture and precipitation fields, which are critical for convective coupling.

In summary, deficiencies in CCEW representation are not attributable to a single factor but rather a combination of resolution, parameterized convection design, and representation of background state. The clearest gains arise from explicitly resolving deep convection, with further improvements possible through improved convective schemes, bias reduction in the tropical mean state, and reducing or eliminating errors associated with the parent model.

b. A practical guide for forecasters on monitoring equatorial waves

Since NWP models often struggle with accurate local-scale rainfall predictions in the tropics, operational forecasters commonly use the following approaches:

- The meteorological "object" approach: This enables the tracking of cyclonic patterns (for Rossby and MRG waves) or wet anomalies (for Kelvin waves) over time and space, helping to focus on key atmospheric features rather than raw rainfall predictions.
- Predictable parameters: Forecasters rely on variables with higher and longer predictability than rainfall, such as precipitable water (PW) or velocity potential (VP), to gain insights into atmospheric dynamics.

The meteorological object approach plays a central role in operational forecasting, allowing forecasters to conceptualize weather in terms of types and sequences of homogeneous anomalies, such as dry or wet spells. Even when numerical predictions perform well, this approach supports clearer communication of forecast information to users. By extracting relevant space–time scales from a seamlessly predicted "movie" of weather patterns, forecasters can tailor their communication to meet user needs and aid decision-making effectively.

In practice, forecasters analyze traditional fields such as streamlines, wind, humidity, and vorticity, alongside advanced products like precipitable water, layer-averaged humidity, and wet-bulb potential temperature. In tropical regions, where day-to-day weather variability is relatively weak compared to the midlatitudes, forecasters often create their own climatological reference points to identify important weather patterns. To enhance forecasting accuracy and ensure objective analysis, we recommend analyzing daily or weekly anomalies in addition to the raw data. This approach helps identify any deviations from the climatological norms, ranging from synoptic features such as cyclonic circulations to broader patterns such as the monsoon trough.

After examining both the raw data and anomalies, our recommended methodology (Table 2) follows the funnel concept, a stepwise approach that progresses from large-scale to small-scale phenomena. The methodology begins with low-frequency variability (step 1: ENSO and IOD) and then moves to intraseasonal scales (step 2: MJO), followed by synoptic-scale equatorial waves (steps 3–6: CCERWs, CCKWs, MRG, and TD-type disturbances). Step 7 synthesizes the contributions from all waves to understand their combined and potentially nonlinear effects on precipitation, while step 8 connects these wave diagnostics to traditional operational forecasting products and phenomena such as cold surges or monsoon phases. This hierarchical approach helps forecasters systematically identify the dominant drivers of precipitation at progressively finer scales.

For each weather driver, it is important to analyze its contribution to several key parameters (such as zonal wind, outgoing longwave radiation, and precipitable water) individually, rather than relying solely on preconstructed indices or composite charts, which may overlook specific details of the situation being considered (steps 1–6). The use of wave-filtered anomaly data based on forecasts is essential in this process. Additional educational resources provide step-by-step guidance for implementing this framework, including two case study examples that demonstrate the practical application of the funnel concept. For more information, check online

TABLE 2. Recommended framework for analyzing precipitation drivers (funnel concept). Abbreviations: Niño-3.4 = ENSO; DMI = IOD; U/V = zonal/meridional wind; SF = streamfunction; RMM/OMI = MJO indices; BSISO = boreal summer intraseasonal oscillation.

Step	Precipitation driver	Analysis and products	Websites
1	Low frequency (ENSO, IOD)	Niño-3.4, DMI, seasonal VP200, U/V850, SF850, PW maps, low-frequency filters	https://www.bom.gov.au/climate/enso/#tabs=Overview; https://seasonal.meteo.fr
2	MJO	RMM/OMI/BSISO, MJO-filtered maps, 7-day VP200/850, PW, U850, SF850, OLR	https://www.cpc.ncep.noaa.gov/products/precip/CWlink/MJO; https://www.apcc21.org
3–6	CCERW, CCKW, MRG, TD type	ER1/ER2-filtered maps, 1–3-day U850, PW, SF850, OLR, TD phases, and co-occurrence	https://ncics.org/portfolio/monitor/mjo/; https://misva.aeris-data.fr; https://www.bom.gov.au/climate/mjo/
7	Sum of the waves	Recap through Hovmöller diagrams, total anomaly vs wave sum, co-occurrence of waves	
8	Link with total fields	Interaction with cold surges, monsoon bursts/breaks, wet/dry spells	

(https://misva.aeris-data.fr/case-study-2-example-of-forecast-for-feb-2024/).

We recommend utilizing three websites that offer insights into contributions from equatorial waves and interannual modes (low frequency) to the total anomaly. The North Carolina Institute of Climate Studies tropical monitoring website, developed by C. Schreck based on Climate Forecast System subseasonal forecasts (https://ncics.org/portfolio/monitor/mjo), provides contour maps and Hovmöller diagrams at various time scales (from daily to 10-day averages) for all modes or individual equatorial waves. Likewise, the Monitoring and Forecast of Intraseasonal Variability over Africa (MISVA) website (https://misva.aeris-data.fr) developed by Météo-France offers similar products but based on ECMWF subseasonal forecasts and short-range high-resolution data. The wind vector decomposition is a real added value to compare forecasts to climatological patterns. The MISVA website is currently not operational but is likely to become operational in the near future. The third website is the Australian Bureau of Meteorology, which uses its ACCESS-S2 model to offer predictions of tropical atmospheric waves in the form of OLR anomaly maps (http://www.bom.gov.au/climate/mjo/).

A recap (step 7) is necessary to emphasize the leading driver or the co-occurrence of waves, which is crucial for predicting extreme precipitation events. Hovmöller diagrams are particularly useful at this stage. Finally, it is essential to establish the link (step 8) between the modes of variability previously monitored and traditional synoptic features or basinwide patterns observed in total fields. Interactions with phenomena such as cold surges, bursts of westerly winds, trade surges, cyclonic vortices, and tropical cyclone tracks are all part of the comprehensive movie of the forecast.

Additional online resources provide more in-depth discussions of each step to enhance understanding and application. For more information, check online (https://misva.aeris-data.fr/continent-maritime-formation/).

5. Concluding remarks

Rainfall patterns over the MC exhibit a complex multiscale nature, influenced by various factors of weather variability.

Among these factors, equatorial waves emerge as coherent large-scale systems propagating eastward or westward within the tropics, often embedded within and supported by larger-scale convective envelopes such as the MJO, ENSO, and IOD.

Not only these waves directly modulate precipitation through their associated convection and wind patterns, but they also indirectly contribute to precipitation extremes. For instance, CCKWs can intensify the diurnal cycle, while CCERWs and MRGs may supply moisture around their cyclonic circulation, occasionally fueling the development of tropical cyclones. Moreover, these waves can interact nonlinearly with other convectively coupled waves and tropical systems, further exacerbating weather extremes.

Recent studies have underscored the pivotal role of equatorial waves in triggering precipitation extremes across the MC, as highlighted in this review. While equatorial waves and the MJO have been subjects of global forecasting and monitoring for many years, their integration into forecasts specific to the MC is still lacking. Despite some improvements in recent years, significant challenges in forecasting CCEWs and their related rainfall in the MC remain. Amplitude and propagation biases are prominent in current NWP models, which may be reduced in more computationally intensive convection-permitting simulations.

The funnel concept is a recommended framework for analyzing precipitation drivers, investigating how large-scale modes and equatorial waves influence weather patterns across decreasing space–time scales. To improve forecasts, we recommend analyzing the impact of each weather driver on parameters such as zonal wind, outgoing longwave radiation, and precipitable water individually, rather than relying solely on preconstructed indices or composite charts.

Efforts to monitor equatorial waves and the MJO can significantly enhance seamless predictions and aid in identifying dry and wet spells. Thus, incorporating equatorial waves into forecasting methodologies is crucial for advancing our understanding of weather extremes in the MC and mitigating their socioeconomic and environmental impacts.

APPENDIX A

Table of Acronyms

Table A1 provides acronyms and abbreviations used in this manuscript, listed alphabetically.

TABLE A1. List of acronyms and abbreviations.

Acronym	Full name/definition
AI	Artificial intelligence
BMKG	Indonesian Agency for Meteorology, Climatology, and Geophysics
BSISO	Boreal summer intraseasonal oscillation
CCERW	Convectively coupled equatorial Rossby wave
CCEW	Convectively coupled equatorial wave
CCKW	Convectively coupled Kelvin wave
COAMPS	Coupled Ocean–Atmosphere Mesoscale Prediction System
CPD	Cycles per day
DMI	Dipole mode index
ECMWF	European Centre for Medium-Range Weather Forecasts
ENSO	El Niño–Southern Oscillation
EOF	Extended empirical orthogonal function
ERA5	Fifth generation ECMWF atmospheric reanalysis
ERA-Interim	ECMWF interim reanalysis
GPM	Global Precipitation Measurement
IMERG	Integrated Multi-satellitE Retrievals for GPM
IOD	Indian Ocean dipole
MC	Maritime Continent
MJO	Madden–Julian oscillation
MRG	Mixed Rossby–gravity
NWP	Numerical weather prediction
OLR	Outgoing longwave radiation
OMI	OLR-based MJO index
PCF	Parabolic cylinder function
PW	Precipitable water
R2O	Research to operations
RMM	Real-time multivariate MJO
RMSE	Root-mean-square error
S2S	Subseasonal to seasonal
SCSSM	South China Sea summer monsoon
SF	Streamfunction
TD	Tropical depression
UKMO	Met Office
VP	Velocity potential
WACCEM	Water Cycle and Climate Extremes Modeling
WCSSP	Weather and Climate Science for Service Partnership
WWRP	World Weather Research Programme

APPENDIX B

Filtering Criteria for Convectively Coupled Equatorial Wave Identification

Table B1 summarizes the spectral filter settings used to isolate CCKWs and CCERWs from OLR data. The filtering approach is based on zonal wavenumber–frequency decomposition, with additional constraints on phase speed (implicitly via dispersion curves; see Fig. 1) to isolate equatorially trapped wave modes. For details of the filtering procedure, please refer to Matthews (2021, 2025).

For MRG wave identification, we adopt the parabolic cylinder function (PCF) projection method introduced by Yang et al. (2003). In this approach, zonal wind, meridional wind, and geopotential height fields are first filtered in the wavenumber–frequency domain and then projected onto equatorial wave eigenfunctions derived from solutions to the linearized shallow-water equations on an equatorial β plane. These eigenfunctions are represented using PCFs that describe the meridional structure of equatorially trapped waves. Filtering is applied over a broad zonal wavenumbers 2–30 and a frequency range of 0.025–0.5 cycles per day (2–40 days), with no equivalent depth constraints imposed.

TABLE B1. Frequency–zonal wavenumber filter settings for convectively coupled equatorial Kelvin and Rossby waves.

Parameter	CCKWs	CCERWs
Frequency range (cpd)	0.05–0.4	0.016 67–0.4
Period range (days)	2.5–20	2.5–60
Zonal wavenumber range	From +1 to +14	From −10 to −1
Propagation direction	Eastward only	Westward only
Dispersion constraints	$h = 2.5$ and 90-m equivalent depth curves	$h = 2.5$ and 90-m equivalent depth curves

APPENDIX C

Reanalysis Composites for Reforecast Dates

Figure C1 supplements Fig. 17 with GPM-IMERG rainfall composites for GloSea6 and ECMWF reforecast dates.
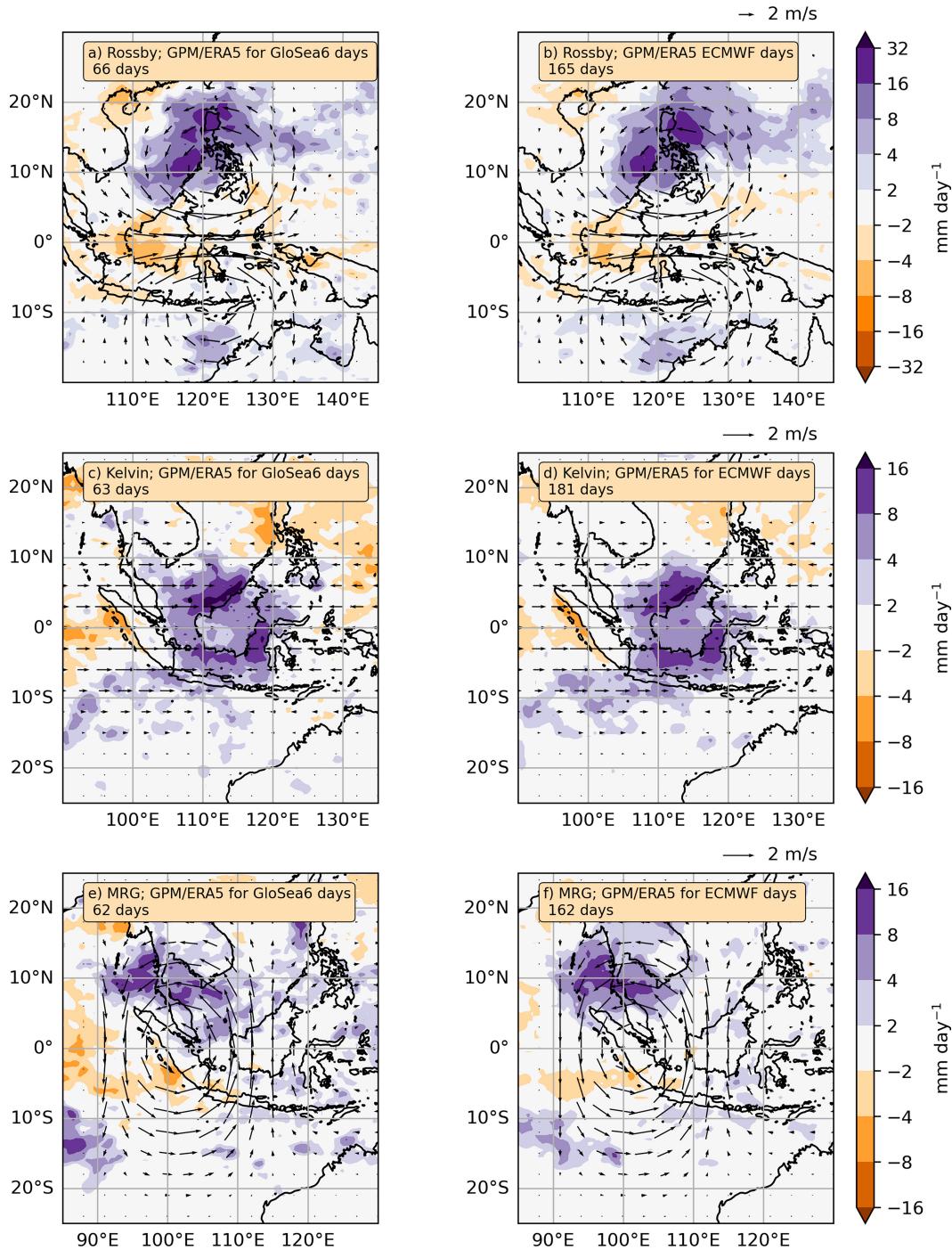
FIG. C1. Supplement to Fig. 17. Daily rainfall anomaly composites for GPM-IMERG for the dates available for (a),(c),(e) GloSea6 reforecast dates and (b),(d),(f) ECMWF reforecast dates. (a),(b) Composites are on days with ERA5 Rossby wave 850-hPa positive vorticity over Philippines (positive vorticity over 120°–125°E), (c),(d) Kelvin wave 850-hPa convergence over Borneo (convergence over 110°–115°E), and (e),(f) MRG 850-hPa positive vorticity over Sumatra (positive vorticity over 100°–105°E). Vectors show the wave-filtered horizontal wind field at 850 hPa using the Yang et al. (2021) method. The total number of events in each composite is shown in the panel title.

REFERENCES

Ahrens, B., and N. Leps, 2021: Sensitivity of convection permitting simulations to lateral boundary conditions in idealized experiments. *J. Adv. Model. Earth Syst.*, **13**, e2021MS002519, https://doi.org/10.1029/2021MS002519.

Aldrian, E., and R. Dwi Susanto, 2003: Identification of three dominant rainfall regions within Indonesia and their relationship to sea surface temperature. *Int. J. Climatol.*, **23**, 1435–1452, https://doi.org/10.1002/joc.950.

Arakawa, A., 2004: The cumulus parameterization problem: Past, present, and future. *J. Climate*, **17**, 2493–2525, https://doi.org/10.1175/1520-0442(2004)017<2493:RATCPP>2.0.CO;2.

——, J.-H. Jung, and C.-M. Wu, 2011: Toward unification of the multiscale modeling of the atmosphere. *Atmos. Chem. Phys.*, **11**, 3731–3742, https://doi.org/10.5194/acp-11-3731-2011.

Argüeso, D., R. Romero, and V. Homar, 2020: Precipitation features of the Maritime Continent in parameterized and explicit convection models. *J. Climate*, **33**, 2449–2466, https://doi.org/10.1175/JCLI-D-19-0416.1.

Aslam, A. A., 2025: Rainfall over the Maritime Continent: Key processes, scale interactions and model representation. *Weather*, **80**, 176–185, https://doi.org/10.1002/wea.7731.

Bai, H., and Coauthors, 2021: Formation of nocturnal offshore rainfall near the west coast of Sumatra: Land breeze or gravity wave? *Mon. Wea. Rev.*, **149**, 715–731, https://doi.org/10.1175/MWR-D-20-0179.1.

Baranowski, D. B., M. K. Flatau, P. J. Flatau, and A. J. Matthews, 2016a: Impact of atmospheric convectively coupled equatorial Kelvin waves on upper ocean variability. *J. Geophys. Res. Atmos.*, **121**, 2045–2059, https://doi.org/10.1002/2015JD024150.

——, ——, ——, and ——, 2016b: Phase locking between atmospheric convectively coupled equatorial Kelvin waves and the diurnal cycle of precipitation over the Maritime Continent. *Geophys. Res. Lett.*, **43**, 8269–8276, https://doi.org/10.1002/2016GL069602.

——, D. E. Waliser, X. Jiang, J. A. Ridout, and M. K. Flatau, 2019: Contemporary GCM fidelity in representing the diurnal cycle of precipitation over the Maritime Continent. *J. Geophys. Res. Atmos.*, **124**, 747–769, https://doi.org/10.1029/2018JD029474.

——, and Coauthors, 2020: Social-media and newspaper reports reveal large-scale meteorological drivers of floods on Sumatra. *Nat. Commun.*, **11**, 2503, https://doi.org/10.1038/s41467-020-16171-2.

Bauer, P., A. Thorpe, and G. Brunet, 2015: The quiet revolution of numerical weather prediction. *Nature*, **525**, 47–55, https://doi.org/10.1038/nature14956.

Bechtold, P., M. Köhler, T. Jung, F. Doblas-Reyes, M. Leutbecher, M. J. Rodwell, F. Vitart, and G. Balsamo, 2008: Advances in simulating atmospheric variability with the ECMWF model: From synoptic to decadal time-scales. *Quart. J. Roy. Meteor. Soc.*, **134**, 1337–1351, https://doi.org/10.1002/qj.289.

——, N. Semane, P. Lopez, J.-P. Chaboureau, A. Beljaars, and N. Bormann, 2014: Representing equilibrium and nonequilibrium convection in large-scale models. *J. Atmos. Sci.*, **71**, 734–753, https://doi.org/10.1175/JAS-D-13-0163.1.

Bengtsson, L., and Coauthors, 2019: Convectively coupled equatorial wave simulations using the ECMWF IFS and the NOAA GFS cumulus convection schemes in the NOAA GFS model. *Mon. Wea. Rev.*, **147**, 4005–4025, https://doi.org/10.1175/MWR-D-19-0195.1.

Bi, K., L. Xie, H. Zhang, X. Chen, X. Gu, and Q. Tian, 2023: Accurate medium-range global weather forecasting with 3D neural networks. *Nature*, **619**, 533–538, https://doi.org/10.1038/s41586-023-06185-3.

Birch, C. E., S. Webster, S. C. Peatman, D. J. Parker, A. J. Matthews, Y. Li, and M. E. E. Hassim, 2016: Scale interactions between the MJO and the western Maritime Continent. *J. Climate*, **29**, 2471–2492, https://doi.org/10.1175/JCLI-D-15-0557.1.

Bougeault, P., and Coauthors, 2010: The THORPEX Interactive Grand Global Ensemble. *Bull. Amer. Meteor. Soc.*, **91**, 1059–1072, https://doi.org/10.1175/2010BAMS2853.1.

Bretherton, C. S., M. E. Peters, and L. E. Back, 2004: Relationships between water vapor path and precipitation over the tropical oceans. *J. Climate*, **17**, 1517–1528, https://doi.org/10.1175/1520-0442(2004)017<1517:RBWVPA>2.0.CO;2.

Chen, G., and R. Huang, 2009: Interannual variations in mixed Rossby–gravity waves and their impacts on tropical cyclogenesis over the western North Pacific. *J. Climate*, **22**, 535–549, https://doi.org/10.1175/2008JCLI2221.1.

Chen, S. S., R. A. Houze, and B. E. Mapes, 1996: Multiscale variability of deep convection in relation to large-scale circulation in TOGA COARE. *J. Atmos. Sci.*, **53**, 1380–1409, https://doi.org/10.1175/1520-0469(1996)053<1380:MVODCI>2.0.CO;2.

Cheng, Y.-M., J. Dias, G. Kiladis, Z. Feng, and L. R. Leung, 2023: Mesoscale convective systems modulated by convectively coupled equatorial waves. *Geophys. Res. Lett.*, **50**, e2023GL103335, https://doi.org/10.1029/2023GL103335.

Clark, P., N. Roberts, H. Lean, S. P. Ballard, and C. Charlton-Perez, 2016: Convection-permitting models: A step-change in rainfall forecasting. *Meteor. Appl.*, **23**, 165–181, https://doi.org/10.1002/met.1538.

Crook, J., and Coauthors, 2024: Impact of the Madden–Julian oscillation and equatorial waves on tracked mesoscale convective systems over Southeast Asia. *Quart. J. Roy. Meteor. Soc.*, **150**, 1724–1751, https://doi.org/10.1002/qj.4667.

Cruz, J. B., J. M. Castanheira, and C. C. DaCamara, 2024: Local identification of equatorial Kelvin waves in real-time operational forecasts. *Quart. J. Roy. Meteor. Soc.*, **150**, 2440–2457, https://doi.org/10.1002/qj.4717.

Da Silva, N. A., and A. J. Matthews, 2021: Impact of the Madden–Julian Oscillation on extreme precipitation over the western Maritime Continent and Southeast Asia. *Quart. J. Roy. Meteor. Soc.*, **147**, 3434–3453, https://doi.org/10.1002/qj.4136.

Derbyshire, S. H., I. Beau, P. Bechtold, J.-Y. Grandpeix, J.-M. Piriou, J.-L. Redelsperger, and P. M. M. Soares, 2004: Sensitivity of moist convection to environmental humidity. *Quart. J. Roy. Meteor. Soc.*, **130**, 3055–3079, https://doi.org/10.1256/qj.03.130.

Dias, J., and G. N. Kiladis, 2016: The relationship between equatorial mixed Rossby–gravity and eastward inertio-gravity waves. Part II. *J. Atmos. Sci.*, **73**, 2147–2163, https://doi.org/10.1175/JAS-D-15-0231.1.

——, M. Gehne, G. N. Kiladis, N. Sakaeda, P. Bechtold, and T. Haiden, 2018: Equatorial waves and the skill of NCEP and ECMWF numerical weather prediction systems. *Mon. Wea. Rev.*, **146**, 1763–1784, https://doi.org/10.1175/MWR-D-17-0362.1.

——, ——, ——, and L. Magnusson, 2023: The role of convectively coupled equatorial waves in sub-seasonal predictions. *Geophys. Res. Lett.*, **50**, e2023GL106198, https://doi.org/10.1029/2023GL106198.

Diong, J.-Y., P. Xavier, S. J. Woolnough, and F. Abdullah, 2023: Equatorial Rossby waves on cold surge days and their impact on rainfall. *Quart. J. Roy. Meteor. Soc.*, **149**, 2031–2047, https://doi.org/10.1002/qj.4493.

Doyle, J. D., C. A. Reynolds, C. Amerault, and J. Moskaitis, 2012: Adjoint sensitivity and predictability of tropical cyclogenesis. *J. Atmos. Sci.*, **69**, 3535–3557, https://doi.org/10.1175/JAS-D-12-0110.1.

——, C. Amerault, C. A. Reynolds, and P. A. Reinecke, 2014: Initial condition sensitivity and predictability of a severe extratropical cyclone using a moist adjoint. *Mon. Wea. Rev.*, **142**, 320–342, https://doi.org/10.1175/MWR-D-13-00201.1.

——, C. A. Reynolds, M. Flatau, and B. Latos, 2023: Sensitivity and predictability of an extreme rainfall event in Sulawesi, Indonesia. *SOLA*, **19A**, 17–26, https://doi.org/10.2151/sola.19A-003.

Feng, X., G.-Y. Yang, K. I. Hodges, and J. Methven, 2023: Equatorial waves as useful precursors to tropical cyclone occurrence and intensification. *Nat. Commun.*, **14**, 511, https://doi.org/10.1038/s41467-023-36055-5.

Fengjin, X., and L. Qiufeng, 2023: An evaluation of vegetation loss due to the super typhoon Sarika in Hainan Island of China. *Nat. Hazards*, **115**, 1677–1695, https://doi.org/10.1007/s11069-022-05613-3.

Ferrett, S., G.-Y. Yang, S. J. Woolnough, J. Methven, K. Hodges, and C. E. Holloway, 2020: Linking extreme precipitation in Southeast Asia to equatorial waves. *Quart. J. Roy. Meteor. Soc.*, **146**, 665–684, https://doi.org/10.1002/qj.3699.

——, J. Methven, S. J. Woolnough, G.-Y. Yang, C. E. Holloway, and G. Wolf, 2023: Hybrid dynamical–statistical forecasts of the risk of rainfall in Southeast Asia dependent on equatorial waves. *Mon. Wea. Rev.*, **151**, 2139–2152, https://doi.org/10.1175/MWR-D-22-0300.1.

Field, P. R., and Coauthors, 2023: Implementation of a double moment cloud microphysics scheme in the UK Met Office regional numerical weather prediction model. *Quart. J. Roy. Meteor. Soc.*, **149**, 703–739, https://doi.org/10.1002/qj.4414.

Fine, C. M., R. H. Johnson, P. E. Ciesielski, and R. K. Taft, 2016: The role of topographically induced vortices in tropical cyclone formation over the Indian Ocean. *Mon. Wea. Rev.*, **144**, 4827–4847, https://doi.org/10.1175/MWR-D-16-0102.1.

Frank, W. M., and P. E. Roundy, 2006: The role of tropical waves in tropical cyclogenesis. *Mon. Wea. Rev.*, **134**, 2397–2417, https://doi.org/10.1175/MWR3204.1.

Gehne, M., and R. Kleeman, 2012: Spectral analysis of tropical atmospheric dynamical variables using a linear shallow-water modal decomposition. *J. Atmos. Sci.*, **69**, 2300–2316, https://doi.org/10.1175/JAS-D-10-05008.1.

——, B. Wolding, J. Dias, and G. N. Kiladis, 2022: Diagnostics of tropical variability for numerical weather forecasts. *Wea. Forecasting*, **37**, 1661–1680, https://doi.org/10.1175/WAF-D-21-0204.1.

Geng, B., and M. Katsumata, 2021: Variation of radar-observed precipitation characteristics in relation to the simultaneous passages of a Madden–Julian oscillation event and convectively coupled equatorial waves during the years of the Maritime Continent pilot study. *Mon. Wea. Rev.*, **149**, 3379–3399, https://doi.org/10.1175/MWR-D-20-0346.1.

Gill, A. E., 1980: Some simple solutions for heat-induced tropical circulation. *Quart. J. Roy. Meteor. Soc.*, **106**, 447–462, https://doi.org/10.1002/qj.49710644905.

——, 1982: *Atmosphere–Ocean Dynamics*. Academic Press, 662 pp.

Goswami, B. B., B. Khouider, R. Phani, P. Mukhopadhyay, and A. Majda, 2017: Improving synoptic and intraseasonal variability in CFSv2 via stochastic representation of organized convection. *Geophys. Res. Lett.*, **44**, 1104–1113, https://doi.org/10.1002/2016GL071542.

Grabowski, W. W., 2003: MJO-like coherent structures: Sensitivity simulations using the cloud-resolving convection parameterization (CRCP). *J. Atmos. Sci.*, **60**, 847–864, https://doi.org/10.1175/1520-0469(2003)060<0847:MLCSSS>2.0.CO;2.

Gruber, A., 1974: The wavenumber-frequency spectra of satellite-measured brightness in the tropics. *J. Atmos. Sci.*, **31**, 1675–1680, https://doi.org/10.1175/1520-0469(1974)031<1675:TWFSOS>2.0.CO;2.

Hannah, W. M., and E. D. Maloney, 2011: The role of moisture–convection feedbacks in simulating the Madden–Julian oscillation. *J. Climate*, **24**, 2754–2770, https://doi.org/10.1175/2011JCLI3803.1.

Hendon, H. H., and B. Liebmann, 1991: The structure and annual variation of antisymmetric fluctuations of tropical convection and their association with Rossby–gravity waves. *J. Atmos. Sci.*, **48**, 2127–2140, https://doi.org/10.1175/1520-0469(1991)048<2127:TSAAVO>2.0.CO;2.

Holloway, C. E., and J. D. Neelin, 2009: Moisture vertical structure, column water vapor, and tropical deep convection. *J. Atmos. Sci.*, **66**, 1665–1683, https://doi.org/10.1175/2008JAS2806.1.

——, S. J. Woolnough, and G. M. S. Lister, 2012: Precipitation distributions for explicit versus parametrized convection in a large-domain high-resolution tropical case study. *Quart. J. Roy. Meteor. Soc.*, **138**, 1692–1708, https://doi.org/10.1002/qj.1903.

Honnert, R., and Coauthors, 2020: The atmospheric boundary layer and the "gray zone" of turbulence: A critical review. *J. Geophys. Res. Atmos.*, **125**, e2019JD030317, https://doi.org/10.1029/2019JD030317.

Hu, P., J. Huangfu, W. Chen, T. Feng, L. Wang, and Y. Tang, 2023: The first observational evidence of a mixed Rossby–gravity wave contribution to triggering the onset process of the South China Sea summer monsoon. *Environ. Res. Lett.*, **18**, 124010, https://doi.org/10.1088/1748-9326/ad07b3.

Huang, P., and R. Huang, 2011: Climatology and interannual variability of convectively coupled equatorial waves activity. *J. Climate*, **24**, 4451–4465, https://doi.org/10.1175/2011JCLI4021.1.

Hung, M.-P., J.-L. Lin, W. Wang, D. Kim, T. Shinoda, and S. J. Weaver, 2013: MJO and convectively coupled equatorial waves simulated by CMIP5 climate models. *J. Climate*, **26**, 6185–6214, https://doi.org/10.1175/JCLI-D-12-00541.1.

Itoh, H., and M. Ghil, 1988: The generation mechanism of mixed Rossby-gravity waves in the equatorial troposphere. *J. Atmos. Sci.*, **45**, 585–604, https://doi.org/10.1175/1520-0469(1988)045<0585:TGMOMR>2.0.CO;2.

Janiga, M. A., J. C. Schreck, J. A. Ridout, M. Flatau, N. P. Barton, E. J. Metzger, and C. A. Reynolds, 2018: Subseasonal forecasts of convectively coupled equatorial waves and the MJO: Activity and predictive skill. *Mon. Wea. Rev.*, **146**, 2337–2360, https://doi.org/10.1175/MWR-D-17-0261.1.

Jia, X., J. Ge, and S. Wang, 2016: Diverse impacts of ENSO on wintertime rainfall over the Maritime Continent. *Int. J. Climatol.*, **36**, 3384–3397, https://doi.org/10.1002/joc.4562.

Jiang, X., and Coauthors, 2009: Vertical heating structures associated with the MJO as characterized by TRMM estimates, ECMWF reanalyses, and forecasts: A case study during 1998/99 winter. *J. Climate*, **22**, 6001–6020, https://doi.org/10.1175/2009JCLI3048.1.

Jones, R. W., C. Sanchez, H. Lewis, J. Warner, S. Webster, and J. Macholl, 2023: Impact of domain size on tropical precipitation within explicit convection simulations. *Geophys. Res. Lett.*, **50**, e2023GL104672, https://doi.org/10.1029/2023GL104672.

Judt, F., 2020: Atmospheric predictability of the tropics, middle latitudes, and polar regions explored through global storm-resolving simulations. *J. Atmos. Sci.*, **77**, 257–276, https://doi.org/10.1175/JAS-D-19-0116.1.

——, and R. Rios-Berrios, 2021: Resolved convection improves the representation of equatorial waves and tropical rainfall variability in a global nonhydrostatic model. *Geophys. Res. Lett.*, **48**, e2021GL093265, https://doi.org/10.1029/2021GL093265.

Karlowska, E., A. J. Matthews, B. G. Webber, T. Graham, and P. Xavier, 2024: Two-way feedback between the Madden–Julian Oscillation and diurnal warm layers in a coupled ocean–atmosphere model. *Quart. J. Roy. Meteor. Soc.*, **150**, 4113–4132, https://doi.org/10.1002/qj.4807.

Kikuchi, K., 2014: An introduction to combined Fourier–wavelet transform and its application to convectively coupled equatorial waves. *Climate Dyn.*, **43**, 1339–1356, https://doi.org/10.1007/s00382-013-1949-8.

——, G. N. Kiladis, J. Dias, and T. Nasuno, 2018: Convectively coupled equatorial waves within the MJO during CINDY/DYNAMO: Slow Kelvin waves as building blocks. *Climate Dyn.*, **50**, 4211–4230, https://doi.org/10.1007/s00382-017-3869-5.

Kiladis, G. N., M. C. Wheeler, P. T. Haertel, K. H. Straub, and P. E. Roundy, 2009: Convectively coupled equatorial waves. *Rev. Geophys.*, **47**, RG2003, https://doi.org/10.1029/2008RG000266.

——, J. Dias, and M. Gehne, 2016: The relationship between equatorial mixed Rossby–gravity and eastward inertio-gravity waves. Part I. *J. Atmos. Sci.*, **73**, 2123–2145, https://doi.org/10.1175/JAS-D-15-0230.1.

Kim, H., 2017: The impact of the mean moisture bias on the key physics of MJO propagation in the ECMWF reforecast. *J. Geophys. Res. Atmos.*, **122**, 7772–7784, https://doi.org/10.1002/2017JD027005.

——, P. J. Webster, V. E. Toma, and D. Kim, 2014: Predictability and prediction skill of the MJO in two operational forecasting systems. *J. Climate*, **27**, 5364–5378, https://doi.org/10.1175/JCLI-D-13-00480.1.

——, M. A. Janiga, and K. Pegion, 2019: MJO propagation processes and mean biases in the SubX and S2S reforecasts. *J. Geophys. Res. Atmos.*, **124**, 9314–9331, https://doi.org/10.1029/2019JD031139.

Klingaman, N. P., and S. J. Woolnough, 2014: Using a case-study approach to improve the Madden–Julian oscillation in the Hadley Centre model. *Quart. J. Roy. Meteor. Soc.*, **140**, 2491–2505, https://doi.org/10.1002/qj.2314.

Knippertz, P., and Coauthors, 2022: The intricacies of identifying equatorial waves. *Quart. J. Roy. Meteor. Soc.*, **148**, 2814–2852, https://doi.org/10.1002/qj.4338.

Lam, R., and Coauthors, 2023: Learning skillful medium-range global weather forecasting. *Science*, **382**, 1416–1421, https://doi.org/10.1126/science.adi2336.

Latos, B., and Coauthors, 2021: Equatorial waves triggering extreme rainfall and floods in southwest Sulawesi, Indonesia. *Mon. Wea. Rev.*, **149**, 1381–1401, https://doi.org/10.1175/MWR-D-20-0262.1.

——, and Coauthors, 2023: The role of tropical waves in the genesis of Tropical Cyclone Seroja in the Maritime Continent. *Nat. Commun.*, **14**, 856, https://doi.org/10.1038/s41467-023-36498-w.

Lawrence, B. N., and Coauthors, 2013: Storing and manipulating environmental big data with JASMIN. *2013 IEEE Int. Conf. on Big Data*, Silicon Valley, CA, Institute of Electrical and Electronics Engineers, 68–75, https://doi.org/10.1109/BigData.2013.6691556.

Li, Y., and S. N. Stechmann, 2020: Predictability of tropical rainfall and waves: Estimates from observational data. *Quart. J. Roy. Meteor. Soc.*, **146**, 1668–1684, https://doi.org/10.1002/qj.3759.

Liebmann, B., H. H. Hendon, and J. D. Glick, 1997: On the generation of two-day convective disturbances across the western equatorial Pacific. *J. Meteor. Soc. Japan*, **75**, 939–946, https://doi.org/10.2151/jmsj1965.75.4_939.

Lin, H., N. Gagnon, S. Beauregard, R. Muncaster, M. Markovic, B. Denis, and M. Charron, 2016: GEPS-based monthly prediction at the Canadian Meteorological Centre. *Mon. Wea. Rev.*, **144**, 4867–4883, https://doi.org/10.1175/MWR-D-16-0138.1.

Lin, J., B. Mapes, M. Zhang, and M. Newman, 2004: Stratiform precipitation, vertical heating profiles, and the Madden–Julian oscillation. *J. Atmos. Sci.*, **61**, 296–309, https://doi.org/10.1175/1520-0469(2004)061<0296:SPVHPA>2.0.CO;2.

——, and Coauthors, 2006: Tropical intraseasonal variability in 14 IPCC AR4 climate models. Part I: Convective signals. *J. Climate*, **19**, 2665–2690, https://doi.org/10.1175/JCLI3735.1.

Liu, X., and Coauthors, 2019: Validity of parameter optimization in improving MJO simulation and prediction using the subseasonal to seasonal forecast model of Beijing Climate Center. *Climate Dyn.*, **52**, 3823–3843, https://doi.org/10.1007/s00382-018-4369-y.

Lopez-Bravo, C., C. L. Vincent, Y. Huang, and T. P. Lane, 2023: A case study of a West Sumatra squall line using satellite observations. *Mon. Wea. Rev.*, **151**, 523–543, https://doi.org/10.1175/MWR-D-21-0194.1.

Lubis, S. W., and C. Jacobi, 2015: The modulating influence of convectively Coupled Equatorial Waves (CCEWs) on the variability of tropical precipitation. *Int. J. Climatol.*, **35**, 1465–1483, https://doi.org/10.1002/joc.4069.

——, and M. R. Respati, 2021: Impacts of convectively coupled equatorial waves on rainfall extremes in Java, Indonesia. *Int. J. Climatol.*, **41**, 2418–2440, https://doi.org/10.1002/joc.6967.

——, and Coauthors, 2022: Record-breaking precipitation in Indonesia's capital of Jakarta in early January 2020 linked to the northerly surge, equatorial waves, and MJO. *Geophys. Res. Lett.*, **49**, e2022GL101513, https://doi.org/10.1029/2022GL101513.

MacLachlan, C., and Coauthors, 2015: Global Seasonal forecast system version 5 (GloSea5): A high-resolution seasonal forecast system. *Quart. J. Roy. Meteor. Soc.*, **141**, 1072–1084, https://doi.org/10.1002/qj.2396.

Madden, R. A., and P. R. Julian, 1972: Description of global-scale circulation cells in the tropics with a 40–50 day period. *J. Atmos. Sci.*, **29**, 1109–1123, https://doi.org/10.1175/1520-0469(1972)029<1109:DOGSCC>2.0.CO;2.

Maher, P., G. K. Vallis, S. C. Sherwood, M. J. Webb, and P. G. Sansom, 2018: The impact of parameterized convection on climatological precipitation in atmospheric global climate models. *Geophys. Res. Lett.*, **45**, 3728–3736, https://doi.org/10.1002/2017GL076826.

Majda, A. J., B. Khouider, G. N. Kiladis, K. H. Straub, and M. G. Shefter, 2004: A model for convectively coupled tropical waves: Nonlinearity, rotation, and comparison with observations. *J.*

Atmos. Sci., **61**, 2188–2205, https://doi.org/10.1175/1520-0469(2004)061<2188:AMFCCT>2.0.CO;2.

Mapes, B., S. Tulich, J. Lin, and P. Zuidema, 2006: The mesoscale convection life cycle: Building block or prototype for large-scale tropical waves? *Dyn. Atmos. Oceans*, **42**, 3–29, https://doi.org/10.1016/j.dynatmoce.2006.03.003.

Mapes, B. E., 2000: Convective inhibition, subgrid-scale triggering energy, and stratiform instability in a toy tropical wave model. *J. Atmos. Sci.*, **57**, 1515–1535, https://doi.org/10.1175/1520-0469(2000)057<1515:cisste>2.0.co;2.

Matsuno, T., 1966: Quasi-geostrophic motions in the equatorial area. *J. Meteor. Soc. Japan*, **44**, 25–43, https://doi.org/10.2151/jmsj1965.44.1_25.

Matthews, A. J., 2021: Dynamical propagation and growth mechanisms for convectively coupled equatorial Kelvin waves over the Indian Ocean. *Quart. J. Roy. Meteor. Soc.*, **147**, 4310–4336, https://doi.org/10.1002/qj.4179.

——, 2025: A vorticity budget for theoretical and convectively coupled equatorial Rossby waves: Dynamical propagation and growth mechanisms. *Quart. J. Roy. Meteor. Soc.*, **151**, e4917, https://doi.org/10.1002/qj.4917.

Measey, M., 2010: Indonesia: A vulnerable country in the face of climate change. *Global Majority Electron.-J.*, **1**, 31–45.

Meehl, G. A., R. Lukas, G. N. Kiladis, K. M. Weickmann, A. J. Matthews, and M. C. Wheeler, 2001: A conceptual framework for time and space scale interactions in the climate system. *Climate Dyn.*, **17**, 753–775, https://doi.org/10.1007/s003820000143.

Moe, I. R., S. Kure, N. F. Januriyadi, M. Farid, K. Udo, S. Kazama, and S. Koshimura, 2017: Future projection of flood inundation considering land-use changes and land subsidence in Jakarta, Indonesia. *Hydrol. Res. Lett.*, **11**, 99–105, https://doi.org/10.3178/hrl.11.99.

Molinari, J., D. Vollaro, and C. J. Schreck III, 2006: Incorporation of equatorial wave modes into tropical synoptic meteorology: Is it worth the trouble? *27th Conf. on Hurricanes and Tropical Meteorology*, Vol. **11**, Monterey, CA, Amer. Meteor. Soc., 11C.1, https://ams.confex.com/ams/27Hurricanes/techprogram/paper_107962.htm.

Moron, V., A. W. Robertson, J.-H. Qian, and M. Ghil, 2015: Weather types across the Maritime Continent: From the diurnal cycle to interannual variations. *Front. Environ. Sci.*, **2**, 65, https://doi.org/10.3389/fenvs.2014.00065.

Muhammad, F. R., S. W. Lubis, and S. Setiawan, 2021: Impacts of the Madden–Julian oscillation on precipitation extremes in Indonesia. *Int. J. Climatol.*, **41**, 1970–1984, https://doi.org/10.1002/joc.6941.

——, C. Vincent, A. King, and S. W. Lubis, 2024: The impacts of convectively coupled equatorial waves on extreme rainfall in northern Australia. *J. Climate*, **37**, 5973–5993, https://doi.org/10.1175/JCLI-D-24-0042.1.

Muis, S., B. Güneralp, B. Jongman, J. C. J. H. Aerts, and P. J. Ward, 2015: Flood risk and adaptation strategies under climate change and urban expansion: A probabilistic analysis using global data. *Sci. Total Environ.*, **538**, 445–457, https://doi.org/10.1016/j.scitotenv.2015.08.068.

Mustafa, J. M., A. J. Matthews, R. A. Hall, K. J. Heywood, and M. V. C. Azaneu, 2025: Modulation of the observed diurnal cycle of precipitation over the Maritime Continent by the Madden-Julian oscillation. *J. Geophys. Res. Atmos.*, **130**, e2024JD042054, https://doi.org/10.1029/2024JD042054.

Nakazawa, T., 1988: Tropical super clusters within intraseasonal variations over the western Pacific. *J. Meteor. Soc. Japan*, **66**, 823–839, https://doi.org/10.2151/jmsj1965.66.6_823.

Nguyen, H., and Coauthors, 2025: Large-scale to local factors influencing Sumatra squalls affecting Singapore. *Climate Dyn.*, **63**, 286, https://doi.org/10.1007/s00382-025-07766-w.

Nur'utami, M. N., and R. Hidayat, 2016: Influences of IOD and ENSO to Indonesian rainfall variability: Role of atmosphere-ocean interaction in the Indo-Pacific sector. *Proc. Environ. Sci.*, **33**, 196–203, https://doi.org/10.1016/j.proenv.2016.03.070.

Peatman, S. C., A. J. Matthews, and D. P. Stevens, 2014: Propagation of the Madden–Julian Oscillation through the Maritime Continent and scale interaction with the diurnal cycle of precipitation. *Quart. J. Roy. Meteor. Soc.*, **140**, 814–825, https://doi.org/10.1002/qj.2161.

——, J. Schwendike, C. E. Birch, J. H. Marsham, A. J. Matthews, and G.-Y. Yang, 2021: A local-to-large scale view of Maritime Continent rainfall: Control by ENSO, MJO, and equatorial waves. *J. Climate*, **34**, 8933–8953, https://doi.org/10.1175/JCLI-D-21-0263.1.

——, C. E. Birch, J. Schwendike, J. H. Marsham, C. Dearden, S. Webster, R. R. Neely, and A. J. Matthews, 2023: The role of density currents and gravity waves in the offshore propagation of convection over Sumatra. *Mon. Wea. Rev.*, **151**, 1757–1777, https://doi.org/10.1175/MWR-D-22-0322.1.

Plant, R. S., and J.-I. Yano, 2015: *Parameterization of Atmospheric Convection (In 2 Volumes)*, Vol. 1. World Scientific, 1172 pp.

Pramuwardani, I., H. Harjo, Sunarto, and A. Sopaheluwakan, 2018: Indonesian rainfall variability during western North Pacific and Australian monsoon phase related to convectively coupled equatorial waves. *Arab. J. Geosci.*, **11**, 673, https://doi.org/10.1007/s12517-018-4003-7.

Price, I., and Coauthors, 2025: Probabilistic weather forecasting with machine learning. *Nature*, **637**, 84–90, https://doi.org/10.1038/s41586-024-08252-9.

Rakhman, S., S. W. Lubis, and S. Setiawan, 2017: Impact of ENSO on seasonal variations of Kelvin Waves and mixed Rossby-Gravity Waves. *IOP Conf. Ser.: Earth Environ. Sci.*, **54**, 012035, https://doi.org/10.1088/1755-1315/54/1/012035.

Randall, D., M. Khairoutdinov, A. Arakawa, and W. Grabowski, 2003: Breaking the cloud parameterization deadlock. *Bull. Amer. Meter. Soc.*, **84**, 1547–1564, https://doi.org/10.1175/BAMS-84-11-1547.

Reichstein, M., G. Camps-Valls, B. Stevens, M. Jung, J. Denzler, N. Carvalhais, and F. Prabhat, 2019: Deep learning and process understanding for data-driven Earth system science. *Nature*, **566**, 195–204, https://doi.org/10.1038/s41586-019-0912-1.

Richter, J. H., and P. J. Rasch, 2008: Effects of convective momentum transport on the atmospheric circulation in the community atmosphere model, version 3. *J. Climate*, **21**, 1487–1499, https://doi.org/10.1175/2007JCLI1789.1.

Roundy, P. E., 2008: Analysis of convectively coupled Kelvin waves in the Indian Ocean MJO. *J. Atmos. Sci.*, **65**, 1342–1359, https://doi.org/10.1175/2007JAS2345.1.

——, 2012: Observed structure of convectively coupled waves as a function of equivalent depth: Kelvin waves and the Madden–Julian oscillation. *J. Atmos. Sci.*, **69**, 2097–2106, https://doi.org/10.1175/JAS-D-12-03.1.

Ruppert, J. H., and F. Zhang, 2019: Diurnal forcing and phase locking of gravity waves in the Maritime Continent. *J. Atmos. Sci.*, **76**, 2815–2835, https://doi.org/10.1175/JAS-D-19-0061.1.

Saji, N. H., B. N. Goswami, P. N. Vinayachandran, and T. Yamagata, 1999: A dipole mode in the tropical Indian Ocean. *Nature*, **401**, 360–363, https://doi.org/10.1038/43854.

Sakaeda, N., G. Kiladis, and J. Dias, 2020: The diurnal cycle of rainfall and the convectively coupled equatorial waves over the Maritime Continent. *J. Climate*, **33**, 3307–3331, https://doi.org/10.1175/JCLI-D-19-0043.1.

Satoh, M., B. Stevens, F. Judt, M. Khairoutdinov, S.-J. Lin, W. M. Putman, and P. Düben, 2019: Global cloud-resolving models. *Curr. Climate Change Rep.*, **5**, 172–184, https://doi.org/10.1007/s40641-019-00131-0.

Saufina, E., and Coauthors, 2025: The role of Madden-Julian oscillation, westerly wind bursts, and Kelvin waves in triggering extreme rainfall through Mesoscale Convective Systems: A case study of West Sumatra, March 7–8, 2024. *Atmos. Res.*, **318**, 107993, https://doi.org/10.1016/j.atmosres.2025.107993.

Schott, F. A., S.-P. Xie, and J. P. McCreary, Jr., 2009: Indian Ocean circulation and climate variability. *Rev. Geophys.*, **47**, RG1002, https://doi.org/10.1029/2007RG000245.

Schreck, C. J., J. Molinari, and K. I. Mohr, 2011: Attributing tropical cyclogenesis to equatorial waves in the western North Pacific. *J. Atmos. Sci.*, **68**, 195–209, https://doi.org/10.1175/2010JAS3396.1.

——, M. A. Janiga, and S. Baxter, 2020: Sources of tropical subseasonal skill in the CFSv2. *Mon. Wea. Rev.*, **148**, 1553–1565, https://doi.org/10.1175/MWR-D-19-0289.1.

Senior, N. V., A. J. Matthews, B. G. M. Webber, S. Webster, R. W. Jones, D. S. Permana, J. A. I. Paski, and R. Fadila, 2023: Extreme precipitation at Padang, Sumatra triggered by convectively coupled Kelvin waves. *Quart. J. Roy. Meteor. Soc.*, **149**, 2281–2300, https://doi.org/10.1002/qj.4506.

——, ——, ——, J. A. I. Paski, D. E. Nuryanto, R. W. Jones, D. S. Permana, and A. H. Febriyanti, 2025: Abrupt ending of the Madden–Julian Oscillation by convectively coupled Kelvin wave precipitation leaves a swath of flooding across Indonesia. *Quart. J. Roy. Meteor. Soc.*, **151**, e4997, https://doi.org/10.1002/qj.4997.

Sherwood, S. C., 1999: Convective precursors and predictability in the tropical western Pacific. *Mon. Wea. Rev.*, **127**, 2977–2991, https://doi.org/10.1175/1520-0493(1999)127<2977:CPAPIT>2.0.CO;2.

Short, C. J., and J. Petch, 2022: Reducing the spin-up of a regional NWP system without data assimilation. *Quart. J. Roy. Meteor. Soc.*, **148**, 1623–1643, https://doi.org/10.1002/qj.4268.

Stevens, B., and Coauthors, 2019: DYAMOND: The DYnamics of the Atmospheric general circulation Modeled On Non-hydrostatic Domains. *Prog. Earth Planet. Sci.*, **6**, 61, https://doi.org/10.1186/s40645-019-0304-z.

Straub, K. H., and G. N. Kiladis, 2003: The observed structure of convectively coupled Kelvin waves: Comparison with simple models of coupled wave instability. *J. Atmos. Sci.*, **60**, 1655–1668, https://doi.org/10.1175/1520-0469(2003)060<1655:TOSOCC>2.0.CO;2.

——, P. T. Haertel, and G. N. Kiladis, 2010: An analysis of convectively coupled Kelvin waves in 20 WCRP CMIP3 global coupled climate models. *J. Climate*, **23**, 3031–3056, https://doi.org/10.1175/2009JCLI3422.1.

Suhas, E., and J. M. Neena, 2025: Convectively coupled equatorial waves. *Atmospheric Oscillations*, B. Guan, Ed., Elsevier, 99–118, https://doi.org/10.1016/B978-0-443-15638-0.00005-8.

Takayabu, Y. N., 1994: Large-scale cloud disturbances associated with equatorial waves: Part II westward-propagating inertio-gravity waves. *J. Meteor. Soc. Japan*, **72**, 451–465, https://doi.org/10.2151/jmsj1965.72.3_451.

Tomassini, L., and Coauthors, 2023: Confronting the convective gray zone in the global configuration of the Met Office Unified Model. *J. Adv. Model. Earth Syst.*, **15**, e2022MS003418, https://doi.org/10.1029/2022MS003418.

Trismidianto, and Coauthors, 2023: Interactions among Cold Surge, Cross-Equatorial Northerly Surge, and Borneo Vortex in influencing extreme rainfall during Madden–Julian oscillation over the Indonesia Maritime Continent. *Meteor. Atmos. Phys.*, **135**, 43, https://doi.org/10.1007/s00703-023-00978-x.

Tung, W.-W., and M. Yanai, 2002: Convective momentum transport observed during the TOGA COARE IOP. Part I: General features. *J. Atmos. Sci.*, **59**, 1857–1871, https://doi.org/10.1175/1520-0469(2002)059<1857:CMTODT>2.0.CO;2.

van der Linden, R., A. H. Fink, J. G. Pinto, T. Phan-Van, and G. N. Kiladis, 2016: Modulation of daily rainfall in southern Vietnam by the Madden–Julian oscillation and convectively coupled equatorial waves. *J. Climate*, **29**, 5801–5820, https://doi.org/10.1175/JCLI-D-15-0911.1.

Vitart, F., and Coauthors, 2017: The Subseasonal to Seasonal (S2S) Prediction project database. *Bull. Amer. Meteor. Soc.*, **98**, 163–173, https://doi.org/10.1175/BAMS-D-16-0017.1.

Warner, J. L., J. Petch, C. J. Short, and C. Bain, 2023: Assessing the impact of a NWP warm-start system on model spin-up over tropical Africa. *Quart. J. Roy. Meteor. Soc.*, **149**, 621–636, https://doi.org/10.1002/qj.4429.

Warner, T. T., 2010: *Numerical Weather and Climate Prediction.* Cambridge University Press, 550 pp.

Weber, N. J., C. F. Mass, and D. Kim, 2020: The impacts of horizontal grid spacing and cumulus parameterization on subseasonal prediction in a global convection-permitting model. *Mon. Wea. Rev.*, **148**, 4747–4765, https://doi.org/10.1175/MWR-D-20-0171.1.

Wheeler, M., and G. N. Kiladis, 1999: Convectively coupled equatorial waves: Analysis of clouds and temperature in the wavenumber–frequency domain. *J. Atmos. Sci.*, **56**, 374–399, https://doi.org/10.1175/1520-0469(1999)056<0374:ccewao>2.0.co;2.

——, and K. M. Weickmann, 2001: Real-time monitoring and prediction of modes of coherent synoptic to intraseasonal tropical variability. *Mon. Wea. Rev.*, **129**, 2677–2694, https://doi.org/10.1175/1520-0493(2001)129<2677:rtmapo>2.0.co;2.

——, G. N. Kiladis, and P. J. Webster, 2000: Large-scale dynamical fields associated with convectively coupled equatorial waves. *J. Atmos. Sci.*, **57**, 613–640, https://doi.org/10.1175/1520-0469(2000)057<0613:LSDFAW>2.0.CO;2.

Wheeler, M. C., and H. H. Hendon, 2004: An all-season real-time multivariate MJO index: Development of an index for monitoring and prediction. *Mon. Wea. Rev.*, **132**, 1917–1932, https://doi.org/10.1175/1520-0493(2004)132<1917:AARMMI>2.0.CO;2.

——, and H. Nguyen, 2025: Tropical meteorology: Equatorial waves. *Encyclopedia of Atmospheric Sciences*, G. North, F. Zhang, and J. Pyle, Eds., Elsevier, 151–164, https://doi.org/10.1016/b978-0-323-96026-7.00193-4.

Wilks, D. S., 2016: "The stippling shows statistically significant grid points": How research results are routinely overstated and overinterpreted, and what to do about it. *Bull. Amer. Meteor. Soc.*, **97**, 2263–2273, https://doi.org/10.1175/BAMS-D-15-00267.1.

Wolf, G., S. Ferrett, J. Methven, T. H. A. Frame, C. E. Holloway, O. Martinez-Alvarado, and S. J. Woolnough, 2024: Comparison

of probabilistic forecasts of extreme precipitation for a global and convection-permitting ensemble and hybrid statistical–dynamical method based on equatorial wave information. *Quart. J. Roy. Meteor. Soc.*, **150**, 877–896, https://doi.org/10.1002/qj.4627.

Yamamoto, K., T. Sayama, and Apip, 2021: Impact of climate change on flood inundation in a tropical river basin in Indonesia. *Prog. Earth Planet. Sci.*, **8**, 5, https://doi.org/10.1186/s40645-020-00386-4.

Yamanaka, M. D., 2016: Physical climatology of Indonesian Maritime Continent: An outline to comprehend observational studies. *Atmos. Res.*, **178–179**, 231–259, https://doi.org/10.1016/j.atmosres.2016.03.017.

——, S.-Y. Ogino, P.-M. Wu, H. Jun-Ichi, S. Mori, J. Matsumoto, and F. Syamsudin, 2018: Maritime Continent coastlines controlling Earth's climate. *Prog. Earth Planet. Sci.*, **5**, 21, https://doi.org/10.1186/s40645-018-0174-9.

Yanai, M., and T. Maruyama, 1966: Stratospheric wave disturbances propagating over the equatorial Pacific. *J. Meteor. Soc. Japan*, **44**, 291–294, https://doi.org/10.2151/jmsj1965.44.5_291.

Yang, G.-Y., and B. J. Hoskins, 2016: ENSO-related variation of equatorial MRG and Rossby waves and forcing from higher latitudes. *Quart. J. Roy. Meteor. Soc.*, **142**, 2488–2504, https://doi.org/10.1002/qj.2842.

——, B. Hoskins, and J. Slingo, 2003: Convectively coupled equatorial waves: A new methodology for identifying wave structures in observational data. *J. Atmos. Sci.*, **60**, 1637–1654, https://doi.org/10.1175/1520-0469(2003)060<1637:CCEWAN>2.0.CO;2.

——, J. Slingo, and B. Hoskins, 2009: Convectively coupled equatorial waves in high-resolution Hadley Centre climate models. *J. Climate*, **22**, 1897–1919, https://doi.org/10.1175/2008JCLI2630.1.

——, S. Ferrett, S. Woolnough, J. Methven, and C. Holloway, 2021: Real-time identification of equatorial waves and evaluation of waves in global forecasts. *Wea. Forecasting*, **36**, 171–193, https://doi.org/10.1175/WAF-D-20-0144.1.

——, X. Feng, and K. Hodges, 2023: Seasonal and interannual variation of equatorial waves in ERA5 and GloSea5. *Quart. J. Roy. Meteor. Soc.*, **149**, 1109–1134, https://doi.org/10.1002/qj.4460.

Ying, Y., and F. Zhang, 2017: Practical and intrinsic predictability of multiscale weather and convectively coupled equatorial waves during the active phase of an MJO. *J. Atmos. Sci.*, **74**, 3771–3785, https://doi.org/10.1175/JAS-D-17-0157.1.

Yoneyama, K., and C. Zhang, 2020: Years of the Maritime Continent. *Geophys. Res. Lett.*, **47**, e2020GL087182, https://doi.org/10.1029/2020GL087182.

Yu, H., R. H. Johnson, P. E. Ciesielski, and H.-C. Kuo, 2018: Observation of quasi-2-day convective disturbances in the equatorial Indian Ocean during DYNAMO. *J. Atmos. Sci.*, **75**, 2867–2888, https://doi.org/10.1175/JAS-D-17-0351.1.

Žagar, N., J. Tribbia, J. L. Anderson, and K. Raeder, 2009: Uncertainties of estimates of inertia–gravity energy in the atmosphere. Part I: Intercomparison of four analysis systems. *Mon. Wea. Rev.*, **137**, 3837–3857, https://doi.org/10.1175/2009MWR2815.1.

Zängl, G., D. Reinert, P. Rípodas, and M. Baldauf, 2015: The ICON (ICOsahedral Non-hydrostatic) modelling framework of DWD and MPI-M: Description of the non-hydrostatic dynamical core. *Quart. J. Roy. Meteor. Soc.*, **141**, 563–579, https://doi.org/10.1002/qj.2378.

Zhang, G. J., and X. Wu, 2003: Convective momentum transport and perturbation pressure field from a cloud-resolving model simulation. *J. Atmos. Sci.*, **60**, 1120–1139, https://doi.org/10.1175/1520-0469(2003)060<1120:CMTAPP>2.0.CO;2.

Zhang, T., S. Yang, X. Jiang, and P. Zhao, 2016: Seasonal–interannual variation and prediction of wet and dry season rainfall over the Maritime Continent: Roles of ENSO and monsoon circulation. *J. Climate*, **29**, 3675–3695, https://doi.org/10.1175/JCLI-D-15-0222.1.

Zhou, L., R. B. Neale, M. Jochum, and R. Murtugudde, 2012: Improved Madden–Julian oscillations with improved physics: The impact of modified convection parameterizations. *J. Climate*, **25**, 1116–1136, https://doi.org/10.1175/2011JCLI4059.1.

Zhou, X., and B. Wang, 2007: Transition from an eastern Pacific upper-level mixed Rossby-gravity wave to a western Pacific tropical cyclone. *Geophys. Res. Lett.*, **34**, L24801, https://doi.org/10.1029/2007GL031831.

——, and Coauthors, 2022: The development of the NCEP Global Ensemble Forecast System version 12. *Wea. Forecasting*, **37**, 1069–1084, https://doi.org/10.1175/WAF-D-21-0112.1.

Zhu, Y., and T. Li, 2021: Dynamic and thermodynamic modulations of the convectively coupled equatorial waves by the MJO. *Environ. Res. Commun.*, **3**, 025004, https://doi.org/10.1088/2515-7620/abeafa.